Correlative light and electron microscopy reveals the fine circuit structure underlying evidence accumulation in larval zebrafish

Authors

Jonathan Boulanger-Weill[1,2,8,9], Florian Kämpf[4,8], Gregor F. P. Schuhknecht[1,8], Richard L. Schalek[1], Mariela Petkova[1], Sumit Kumar Vohra[5], Yuelong Wu[1], Jay H. Savaliya[1], Robert Tiller[1], Kristian J. Herrera[1], Heike Naumann[4], Maren Eberle[1], Simone Rencken[1], Moritz Stingl[1], Alina Hebling[1], Dana Hockling[1], Katja Slangewal[3,4,10], Zixuan Deng[1], Ruohong C. Wang[1], Lauren L. Zhang[1], Kim N. Kirchberger[4], Isaac H. Bianco[6], Daniel Baum[5], Filippo Del Bene[2,7], Florian Engert[1,7], Jeff W. Lichtman[1,7], Armin Bahl[3,4,7,9,10]

Affiliations

1: Department of Molecular and Cellular Biology, Faculty of Arts and Sciences, Harvard University, Cambridge, MA 02138, USA

2: Sorbonne Université, CNRS, Inserm, Institut de la Vision, F-75012 Paris, France

3: Centre for the Advanced Study of Collective Behaviour, University of Konstanz, Konstanz, Germany

4: Department of Biology, University of Konstanz, Konstanz, Germany

5: Department of Visual and Data-Centric Computing, Zuse Institute Berlin (ZIB), Berlin, Germany

6: Department of Neuroscience, Physiology & Pharmacology, University College London, London, United Kingdom

7: These authors jointly supervised this work: Filippo Del Bene, Florian Engert, Jeff W. Lichtman, Armin Bahl

8: These authors contributed equally: Jonathan Boulanger-Weill, Florian Kämpf, Gregor F. P. Schuhknecht

9: Corresponding authors: boulangerweill@fas.harvard.edu; armin.bahl@uni-konstanz.de

10: International Max Planck Research School QBEE, Konstanz, Germany

Abstract

Evidence accumulation is a fundamental neural computation essential for adaptive behavior, yet its synaptic implementation remains unclear. Addressing this challenge critically depends on linking neural dynamics to circuit structure within the same brain. Here, we combine functional calcium imaging with large-scale ultrastructural electron microscopy (EM) to uncover the wiring logic of visual evidence accumulation in larval zebrafish. In a functionally imaged EM dataset of the anterior hindbrain, we identify conserved morphological cell types whose activity patterns define distinct computational roles. Bilateral inhibition, disinhibition, and recurrent connectivity emerge as key circuit motifs shaping these dynamics. To generalize our findings across animals, we develop a photoconversion-based pipeline to label and reconstruct functionally characterized neurons, enabling us to train a classifier that predicts functional identity from morphology alone. Applying this classifier to a second, whole-brain EM dataset lacking functional data reveals matching connectivity patterns, significantly augmenting its applicability for detailed circuit dissections. Based on these results, we develop and constrain a biophysically realistic neural network model that captures observed dynamics and yields predictions we tested and confirmed experimentally. Our work illustrates how hypothesis-driven connectomics can uncover the synaptic basis of sensory-motor computations and establishes a novel framework for cross-animal circuit dissection in the vertebrate brain.

Introduction

In natural environments, behaviorally relevant signals are often noisy, fragmented, or conflicting. To navigate this complexity and make reliable decisions, animals must continuously accumulate sensory information across space and time. This fundamental computation for selecting appropriate actions has been observed in a wide range of species, including flies (Groschner *et al.*, 2018), fish (Bahl and Engert, 2020; Dragomir, Štih and Portugues, 2020), rodents (Hanks *et al.*, 2015), and primates (Katz *et al.*, 2016). A classic approach for studying this process is through random dot motion stimuli, where some flickering dots move coherently while others are randomly redrawn across the visual field. This stimulus has been used alongside single-neuron and population-level recordings to reveal ramping neural responses, with slopes correlated with coherence levels, indicative of sensory accumulation of evidence (Newsome, Britten and Movshon, 1989; Hanks and Summerfield, 2017). Recent findings suggest that this integration is distributed throughout the mammalian brain, involving both cortical and subcortical regions (Brody and Hanks, 2016). However, the detailed architecture, both at the synaptic and whole-brain levels, that transforms noisy sensory input into discrete motor actions in vertebrates remains unclear.

The zebrafish larva (*Danio rerio*) also responds to random dot motion, accumulating visual evidence of self-motion before initiating stabilizing motor commands (Bahl and Engert, 2020; Dragomir, Štih and Portugues, 2020). Its compact brain and genetic amenability make it a powerful model for investigating neural computations using light microscopy, enabling whole-brain functional circuit dissection that is not feasible in larger vertebrates. Previous research has highlighted the anterior hindbrain, where neurons display calcium dynamics indicative of visual evidence accumulation, as a key computational hub for this process (Bahl and Engert, 2020; Dragomir, Štih and Portugues, 2020). Several network predictions have been proposed: hindbrain neurons accumulate visual input from pretectal (Pt) regions by recurrent connectivity of excitatory neurons, generating persistent activity (Yang *et al.*, 2023). Faster-dynamics neurons in this region were suggested to establish a decision boundary, filtering out low-quality stimuli by inhibiting premature motor activation (Bahl and Engert, 2020). Originating from this area, motor command neurons provide excitatory and inhibitory inputs to distinct pools of reticulospinal neuron subtypes, each tuned to specific movement directions, thereby selecting the appropriate motor output (Orger *et al.*, 2008; Kubo *et al.*, 2014a; Naumann *et al.*, 2016).

Volumetric electron microscopy techniques have made it possible to map synaptic connectivity with remarkable resolution in several invertebrate and vertebrate species (Witvliet *et al.*, 2021; Svara *et al.*, 2022; Turner *et al.*, 2022; Dorkenwald *et al.*, 2024; Schlegel *et al.*, 2024; Shapson-Coe *et al.*, 2024). In *Drosophila*, this connectomic data, when combined with complementary methods such as electrophysiology, optogenetics, and behavioral analysis, can refine models of neural networks (Turner-Evans *et al.*, 2020; Ammer *et al.*, 2023), predict neural dynamics (Lappalainen *et al.*, 2024; Shiu *et al.*, 2024), and elucidate the mechanistic basis of behavior (Dombrovski *et al.*, 2023; Shiu *et al.*, 2024). In vertebrates, neurons are far less stereotypic and do not lend themselves as readily to assigning function based on structure. Further, similar functional response types are often scattered across regions, making it difficult to test proposed wiring schemes through sparse connectivity sampling from separate animals. A prime example of such a lack of topographic representation is the zebrafish pretectum, where binocular and monocular neurons are intermingled (Kubo *et al.*, 2014a; Naumann *et al.*, 2016). Nonetheless, recent advances in functional connectomics in this model organism—combining in vivo calcium imaging with subsequent electron microscopy in the same animal—have made it possible to directly link functional neuronal activity with its underlying synaptic connectivity (Wanner and Friedrich, 2020; Friedrich and Wanner, 2021; Vishwanathan *et al.*, 2024). This approach offers unprecedented insights into how connectomic motifs support neuronal responses, sensory processing, and ultimately behavior in the vertebrate brain.

Building on previous work in which we proposed a biophysically plausible circuit model for evidence accumulation in the vertebrate brain (Bahl and Engert, 2020), we now use ground-truth synaptic connectivity to validate and extend this model. Specifically, we generated connectivity matrices from two separate EM volumes. The first dataset, a functional correlated EM (FCLEM) volume, was obtained after functionally imaging the anterior hindbrain during random dot motion stimuli. The second one spans the entire brain, enabling circuit mapping across broader networks, but lacks functional information. To bridge structure and function, we created a library of photoconverted neurons with known activity profiles and used it to train a classifier capable of predicting functional identity from morphology alone. This approach enables assigning functional identities in EM datasets lacking functional imaging. Our reconstructions revealed recurrent excitation, interhemispheric inhibition, and ipsilateral disinhibition as core motifs for evidence accumulation. We propose that this disinhibition motif may play a key role in endowing the network with the ability to respond to a rapidly changing sensory environment while maintaining its ability to slowly filter relevant cues from noisy signals. The updated model not only reproduces key features of the observed network dynamics but also makes testable predictions for novel visual paradigms. These findings refine our understanding of how sensory signals are transformed into motor outputs and establish a generalizable framework for functional circuit dissection in vertebrate brains.

Results

Correlative electron and light microscopy in a neural circuit performing motion integration

To explore the relationship between structure and function in the anterior hindbrain, we first identified neurons based on their functional dynamics using two-photon calcium imaging (**Fig. 1a** and (Bahl and Engert, 2020)). To that end, we used 7 days post-fertilization (dpf) transgenic larvae expressing a nuclear calcium indicator (Dana *et al.*, 2019) under the *elavl3* pan-neuronal promoter and red markers in the main inhibitory neuronal subtype (Satou *et al.*, 2013) as well as in vascular endothelial cells (Fujita *et al.*, 2011), *Tg(elavl3:H2B-GCaMP7f, gad1b:DsRed, kdrl:mCherryCAAX)*. We recorded neuronal responses evoked by left- and rightward-moving dots of 100% coherence in six optical planes spaced by 12 µm along the dorso-ventral axis in a region spanning from the medial optic tectum to the caudal hindbrain. We performed 2D segmentation of the time-averaged recordings using a convolutional neural network (Weigert *et al.*, 2020) to obtain neuron-specific masks (**Methods**). While many diverse neurotransmitter types exist (Higashijima, Mandel and Fetcho, 2004), the transgenic Gad1b+ label allowed us to assign an inhibitory identity to cells, as GABA is the main inhibitory neurotransmitter in the zebrafish brain (Filippi, Mueller and Driever, 2014). Neurons displayed similar calcium dynamics as previously reported (**Extended Data Fig. 1a** and (Bahl and Engert, 2020)). Unbiased clustering revealed three main functional cell types. Based on their dynamics, we named these cells motion integrator (MI), motion onset (MON), and slow motion integrator (SMI) neurons (**Fig. 1b**, **Extended Data Fig. 1a,b,** and **Methods**). Note that we previously used more descriptive labels based on the potential functional role of these cells within the evidence integration task (evidence integrator, dynamic threshold, and motor command neurons, respectively) (Bahl and Engert, 2020). Out of 15017 functionally imaged neurons, we found 618, 108, and 339 neurons of each type, respectively with the largest fraction located in the anterior hindbrain (62%: 358, 24, and 275 neurons of each type, respectively, **Extended Data Fig. 1c** and **Methods**) but also located in the pretectum (Pt), midbrain (Mb) and cerebellum (Cb) as well as other regions. Previous work suggests that the anterior hindbrain performs temporal integration of direction-selective pretectum whole-field motion inputs (Bahl and Engert, 2020). Compatible with these previous observations, we found that a large fraction of neurons in the anterior hindbrain were direction selective (DS) (75.6% of neurons had an absolute DS index>0.5, **Extended Data Fig. 1d)** with generally slower dynamics than their pretectum and midbrain counterparts (**Extended Data Fig. 1e**).

We next used the same larva, fixated it and stained it for EM (Tapia *et al.*, 2012; Hua, Laserstein and Helmstaedter, 2015) (**Methods**). To identify the coordinates of the block containing the relatively small and constrained region of the anterior hindbrain, we used sparse hindbrain electroporations (Boulanger-Weill *et al.*, 2017) and c3pa-GFP photoactivation (Förster *et al.*, 2018) in separate age-matched larvae (**Extended Data Fig. 2a,b**). Additionally, we performed X-ray computed tomography to ensure staining homogeneity and tissue integrity and to target the sectioning to specific neuronal circuits (**Extended Data Fig. 2c–g**).

We next collected 4010 coronal sections using an automated tape ultra-microtome (Hayworth *et al.*, 2014) and performed multi-beam scanning EM (mSEM) at 4 x 4 x ~30 nm resolution (~416 x 265 x 112 µm, spanning from the medial midbrain to rhombomere 3, **Fig. 1c–e**), totaling 51.4TB of imaging data (**Methods**). Volumetric nanometer-precise alignment and connectome reconstruction were performed via a series of largely automated workflows, enabling high-quality neuronal morphology reconstruction ((Turner *et al.*, 2022), **Methods**). To find single-cell correspondences between two-photon and EM imaging, we performed registration using manually placed corresponding landmarks ((Bogovic *et al.*, 2016), **Methods**). This strategy yielded single-cell precision registration even in dense, low-contrast regions of the brain (**Fig. 1d** and **Extended Data Fig. 2h**). Fluorescently labeled blood vessels, which were not used as landmarks for the registration, allowed us to independently confirm the quality of the mapping (**Extended Data Fig. 2h**). Finally, the EM and registered two-photon datasets were uploaded into an online browsing platform (Dorkenwald *et al.*, 2023), enabling collaborative proofreading of morphology and connectivity of functionally identified neurons (**Methods**).

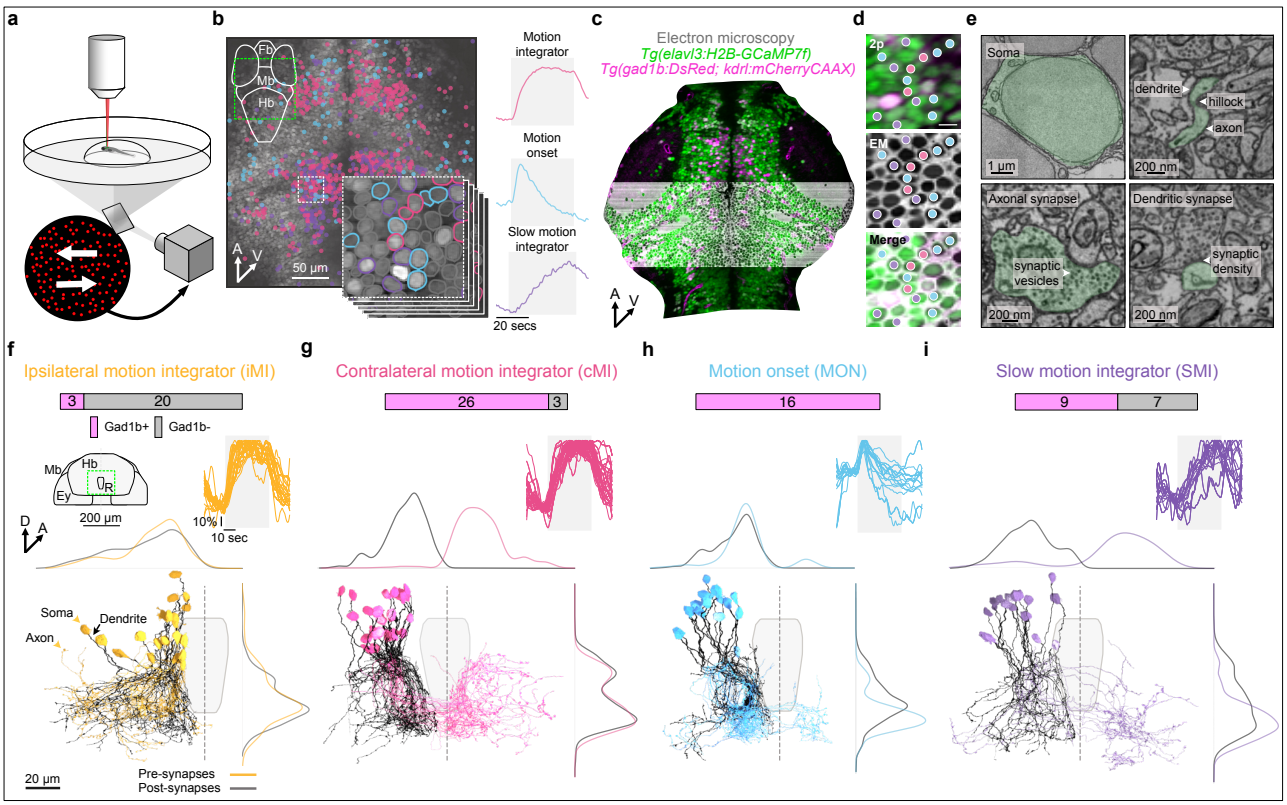

Fig. 1 | Correlative light and electron microscopy of neurons involved in motion evidence integration. a, Schematic of the two-photon imaging setup showing the bottom projection of coherently moving random dots. **b,** Left: spatial distribution of clustered neurons. The background grayscale image represents the average of the six functionally imaged planes. Top-left schematic shows coarse brain organization (dorsal-to-ventral view) and the location of the functionally imaged area (green dashed square). The white dashed square is magnified in the bottom-right snippets, which depict individual planes and are also shown in **(e).** Neurons are circled based on their functional types, while non-clustered neurons are circled in gray. Right: normalized K-means-based regressors used for neuron clustering. Stimulus consists of 0%, 100% (gray shaded area), and 0% coherence. **c,** Single plane of the two-photon image stack mapped to the EM dataset. Magenta

shows inhibitory neurons (Gad1b+) and blood vessels (kdrl+). Green shows nuclear-localized GCaMP7f. Gray indicates the EM dataset. **d,** Detailed alignment between the two-photon imaging (2P) and EM datasets. Scale bar: 5 µm. Neurons from the clustered populations are indicated by colored dots. **e,** EM ultrastructural details of a reconstructed neuron. **f**, Structure-function relationship of functionally imaged and reconstructed neurons in coronal view. Top: distribution of neurotransmitter identity shown as Gad1b-positive (likely inhibitory, magenta) or Gad1b-negative (presumably excitatory, gray). Left: schematic showing coarse brain organization and location of the reconstructed neurons below (green dashed square) and outlines of the raphe (also shown below). Right: traces representing the normalized $\Delta F/F_0$ neuronal activity over time for motion in the preferred direction. Bottom: reconstructed ipsilateral motion integrator (iMI) neurons with somas and axons in orange and dendrites in black. The right neurons are mirrored towards the left hemisphere. The dashed line represents the midline. Surrounding plots are distributions of presynaptic (orange) and postsynaptic (black) synapses along the x (top) and y (right) axes. **g–i,** show identical representation for other neuron types. All neurons and brain regions here and throughout the rest of the paper are registered to a reference brain Atlas. Abbreviations: Mb, midbrain; Hb, hindbrain; R, raphe; Ey, eye; A, anterior; D, dorsal; V, ventral. Neuron-type names, their abbreviations, and associated colors are used throughout the paper.

Structure-function relationship of functionally identified neurons

Within this restricted dataset, encompassing both hemispheres of the anterior hindbrain, we reconstructed 52 MI neurons, 16 MON neurons, and 16 SMI neurons (located in both hemispheres in rhombomeres 1–3) and identified their neurotransmitter identity (**Fig. 1f–i** and **Extended Data Fig. 3a–d**). To probe the connectivity of functionally identified neurons, we trained convolutional neural networks to automatically detect synaptic clefts and assign presynaptic and postsynaptic partner neurons ((Macrina *et al.*, 2021), **Methods** and **Extended Data Fig. 4a–e**).

All of these neurons were unipolar, with the axon emerging from a primary dendrite projecting ventrally, a structure reminiscent of invertebrate neurons (Dorkenwald *et al.*, 2024; Schlegel *et al.*, 2024). We observed distinct patterns among the different functional neuron types: most ipsilateral-projecting MI (iMI) neurons did not express Gad1b (Gad1b-, 20/23) while contralateral-projecting MI (cMI) neurons were mostly Gad1b positive (Gad1b+, 26/29). MON neurons were exclusively Gad1b+ and primarily contralateral-projecting (12/16), whereas SMI neurons exhibited a mix of neurotransmitter and projection types, including 4 ipsilateral-projecting Gad1b+ neurons and 12 contralateral-projecting neurons (9 Gad1b+ and 3 Gad1b-) (**Fig. 1f–i**). iMI neurons were generally positioned closer to the midline compared to other types, with overlapping axons and dendrites (**Fig. 1f** and **Extended Data Fig. 3a**).

In contrast, cMI neurons were located more laterally, displaying clustered dendrites adjacent to the raphe, and had only a few axons leaving the volume (**Fig. 1g** and **Extended Data Fig. 3b**). MON neurons showed tightly clustered dendrites and axons (**Fig. 1h** and **Extended Data Fig. 3c**) with the majority of axonal synapses located on the ipsilateral side. SMI neurons had more dispersed dendrites and axons along both the dorso-ventral and rostro-caudal axes (**Fig. 1i** and **Extended Data Fig. 3d**).

To quantify morphological similarity among neurons, we computed pairwise NBLAST scores using a zebrafish-specific calibration of a previously established method (Costa *et al.*, 2016). NBLAST compares neurons based on their 3D structure and local geometry, enabling clustering across both vertebrate and invertebrate datasets. Hierarchical clustering of these scores revealed clear grouping by functional identity with consistent within-type similarity and distinct between-type boundaries. (**Extended Data Fig. 3e,f**, left). When used as the basis for classification, NBLAST-based clustering achieved an F1-score of ~0.69, indicating that neuronal morphology can partially predict functional type (**Extended Data Fig. 3e,f**, right).

Distinct connectivity motifs across functionally identified neurons in the anterior hindbrain

Starting with the 84 functionally identified reconstructed neurons, we automatically identified a total of 3,218 post-synapses (inputs) and 2,126 pre-synapses (outputs) (**Methods** and **Extended Data Fig.**

4a–e). Among these, 9.59% of randomly selected connected segments were successfully reconstructed (dendrites leading to a soma, or axons leading either to a soma or the edge of the volume), resulting in the identification of 127 additional neurons that had not been functionally imaged (**Fig. 2a**). In addition, we identified 38 truncated axons that did not connect to another neuron. To investigate connectivity motifs we generated a connectivity matrix that included only the 84 functionally identified neurons (**Fig. 2b)** and complemented it with truncated axonal partners terminating within the volume (**Extended Data Fig. 4f**). Distinct connectivity patterns emerged for each neuron type, both at the input and output levels (**Fig 2b–j** and **Extended Data Fig. 4g–r**).

iMI neurons broadly targeted all functional types with a strong preference for MON neurons (35% of synapses, **Fig. 2c**). Notably, approximately 6% of the output synapses targeted iMI neurons, suggesting recurrent connectivity within this neuronal subtype. Additionally, a large fraction of the inputs originated from either the rostral end of the imaged volume or from cMI neurons (22% each, **Fig. 2d** and **Extended Data Fig. 4k**). Previous studies have demonstrated co-activation of anterior hindbrain and pretectum neurons during whole-field visual motion, supporting the existence of anatomical connectivity between these regions (Naumann *et al.*, 2016; Chen *et al.*, 2018). While contributions from other areas cannot be excluded, our findings are consistent with the idea that iMI neurons temporally integrate inputs coming from the pretectum and then relay such signals to other neuron types in the anterior hindbrain.

cMI neurons inhibited all functional types on the contralateral side except MON neurons with a strong bias towards iMI and cMI neurons (22% and 16% respectively, **Fig. 2e**). They received similar amounts of disinhibitory ipsilateral inputs from MON neurons on the ipsilateral side, caudal axonal inputs and disinhibitory inputs from cMI cells on the contralateral hemisphere (15%, 18% and 13% respectively, **Fig. 2f** and **Extended Data Fig. 4l**). These observations provide anatomical confirmation of predicted interhemispheric inhibition within the anterior hindbrain refining turning behavior by processing pretectal inputs (Naumann *et al.*, 2016).

MON neurons targeted cMI neurons ipsilaterally in a disinhibitory manner (18%, **Fig. 2g** and **Extended Data Fig. 4i**) and received mixed inhibitory and excitatory inputs originating from other cells within the anterior hindbrain (41%, **Fig. 2h** and **Extended Data Fig. 4m**).

SMI neurons predominantly targeted caudally projecting neurons with myelinated axons (35%, both ipsilaterally and contralaterally, **Fig. 2i** and **Extended Data Fig. 4j**), suggesting that this cell type might have a role in motor execution, as we have previously proposed (Bahl and Engert, 2020). Consistent with this, one excitatory ipsilateral SMI neuron targeted three Rov3 reticulospinal neurons (**Fig. 2i,** and **Extended Data Fig. 4j,s**), a subtype implicated in lateralized responses to whole-field motion (Orger *et al.*, 2008). SMI neurons received the greatest diversity of inputs, in nearly equal proportions: rostral axonal inputs (12%), caudal axonal inputs (9%), excitation from iMI neurons (7%), ipsilateral inhibition from MON neurons (7%), and contralateral inhibition from cMI neurons (9%, **Fig. 2j** and **Extended Data Fig. 4n**). Interestingly, we did not find any statistical differences between pre- and post-synapses sizes across functionally identified cell types (**Extended Data Fig. 4t,u**), suggesting balanced functional connection weights (Holler *et al.*, 2021) across cell types in the anterior hindbrain.

In summary, our sparse connectomic reconstructions in the hindbrain support a network model of bilateral inhibition across hemispheres mediated by cMI neurons, ipsilateral disinhibition driven by MON neurons, recurrent connectivity within iMI neurons, and direct inputs from SMI neurons to reticulospinal neurons, which drive lateralized movements. To provide the broader scientific community with an online platform to browse neurons from connectomic analyses, we further developed an open-source atlas containing molecular labels and anatomic regions (**Extended Data Fig. 5**, (Vohra et al., in preparation)) to which we uploaded all reconstructed neurons and axonal segments (connected to functionally identified inputs and output partners).

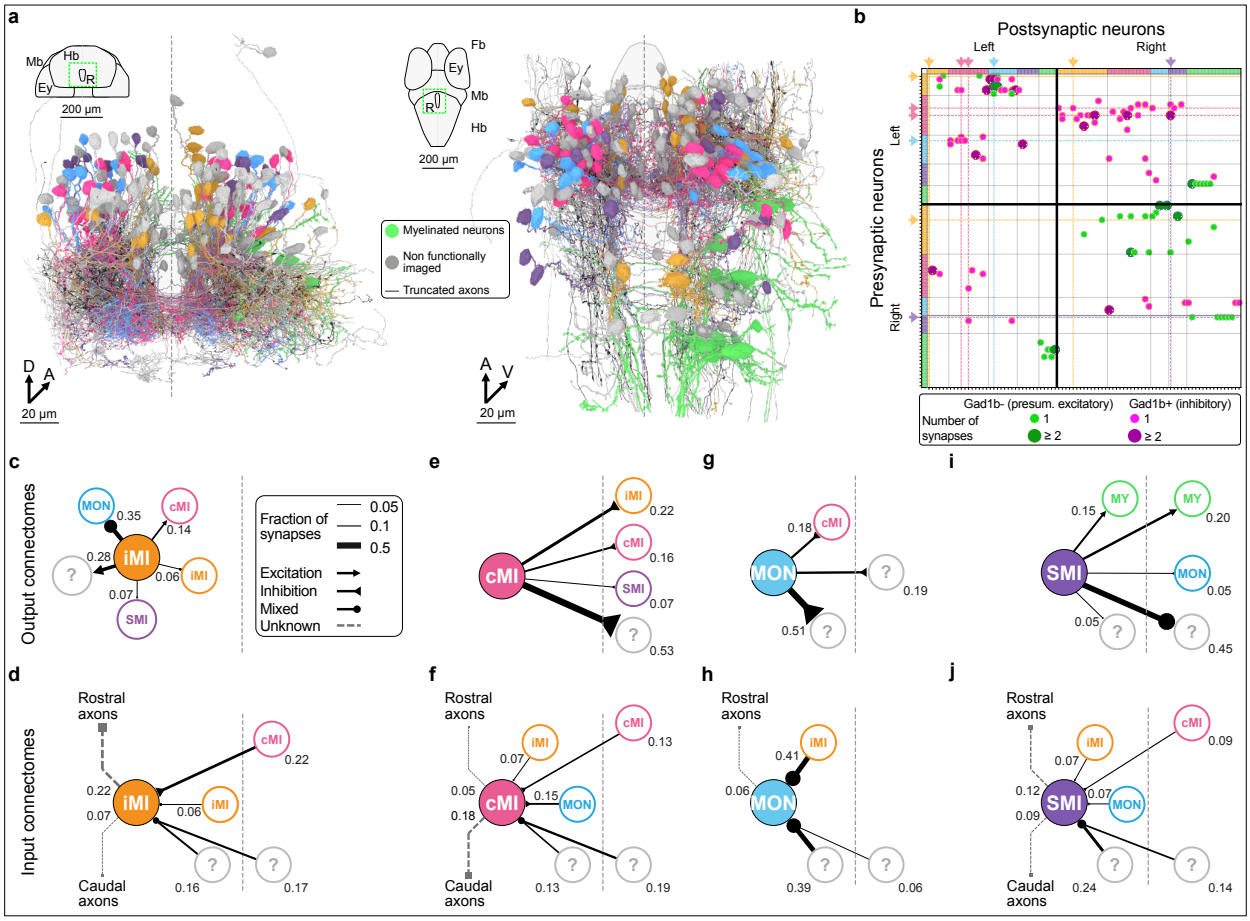

Fig. 2 | Connectomic analyses of functionally identified neuronal subtypes. a, All neurons reconstructed in this study: 84 functionally imaged neurons and connected partners: 38 truncated axons and 127 non-functionally imaged neurons. Left panel: coronal view, right panel: dorsal view. Top schematics show coarse brain organization and location of the reconstructed neurons below (green dashed square) and outlines of the raphe (also shown below). **b,** Connectivity matrix with neurons sorted according to their functional types and hemispheres (thick black bars). Colored arrows and lines correspond to the example connectomes shown in **Extended Data Fig. 4g–n**. Output (**c,e,g,i**) and input (**d,f,h,j**) cell-type connectomes extracted from the connectivity matrix. Connections accounting for less than 5% of the total synapse number are not shown. Question marks represent non-functionally imaged neurons. The dashed line indicates the midline. Abbreviations: Mb, midbrain; Hb, hindbrain; R, raphe; Ey, eye; A, anterior; D, dorsal; V, ventral.

Two-photon-guided characterization of function, anatomy, and neurotransmitter identity

The initial two-photon imaging session was limited to a subset of imaging planes, resulting in a considerable fraction of reconstructed neurons lacking functional information. While NBLAST-based similarity measures provided an initial morphological classification, their performance was only at an F1-score of ~0.69, highlighting the need for more robust strategies. We therefore sought to train supervised classifiers that could reliably predict neuronal functional types based on morphological features beyond NBLAST-based approaches. In the ideal situation, such classifiers may even be trained and tested purely based on light microscopy experiments, which would provide a powerful tool to enhance any, not just our current, EM- and light-based library of anatomical reconstructions. Our FCLEM dataset provides a unique ground truth dataset for understanding the relationship between structure and function across anterior hindbrain cell types, allowing us to validate such classifiers.

In a new set of experiments, we used two-photon excitation of photoactivatable GFP (Patterson and Lippincott-Schwartz, 2002; Förster *et al.*, 2018), to reconstruct the anatomy of functionally characterized neurons (Kramer *et al.*, 2019). We combined this approach with *in-situ* RNA hybridization, HCR FISH (Choi *et al.*, 2018), employing *gad1b* and *vglut2a* probes to selectively label GABAergic (inhibitory) and glutamatergic (excitatory) neurons, respectively (**Fig. 3a**). This strategy

was applied across 47 larvae to generate a comprehensive multi-feature neuronal library that links functional dynamics, anatomy, and neurotransmitter identity—purely based on light microscopy experiments (**Fig. 3b–e**). Neuron functional types were determined through clustering analysis consistent with our FCLEM experiment (**Fig. 1b, Methods**). Patterns observed in these experiments closely mirrored results from our FCLEM dataset (compare **Fig. 3b–e** and **Extended Data Fig. 6a–d** with **Fig. 1f–i** and **Extended Data Fig. 3a–d**), validating the two approaches across multiple animals and imaging modalities.

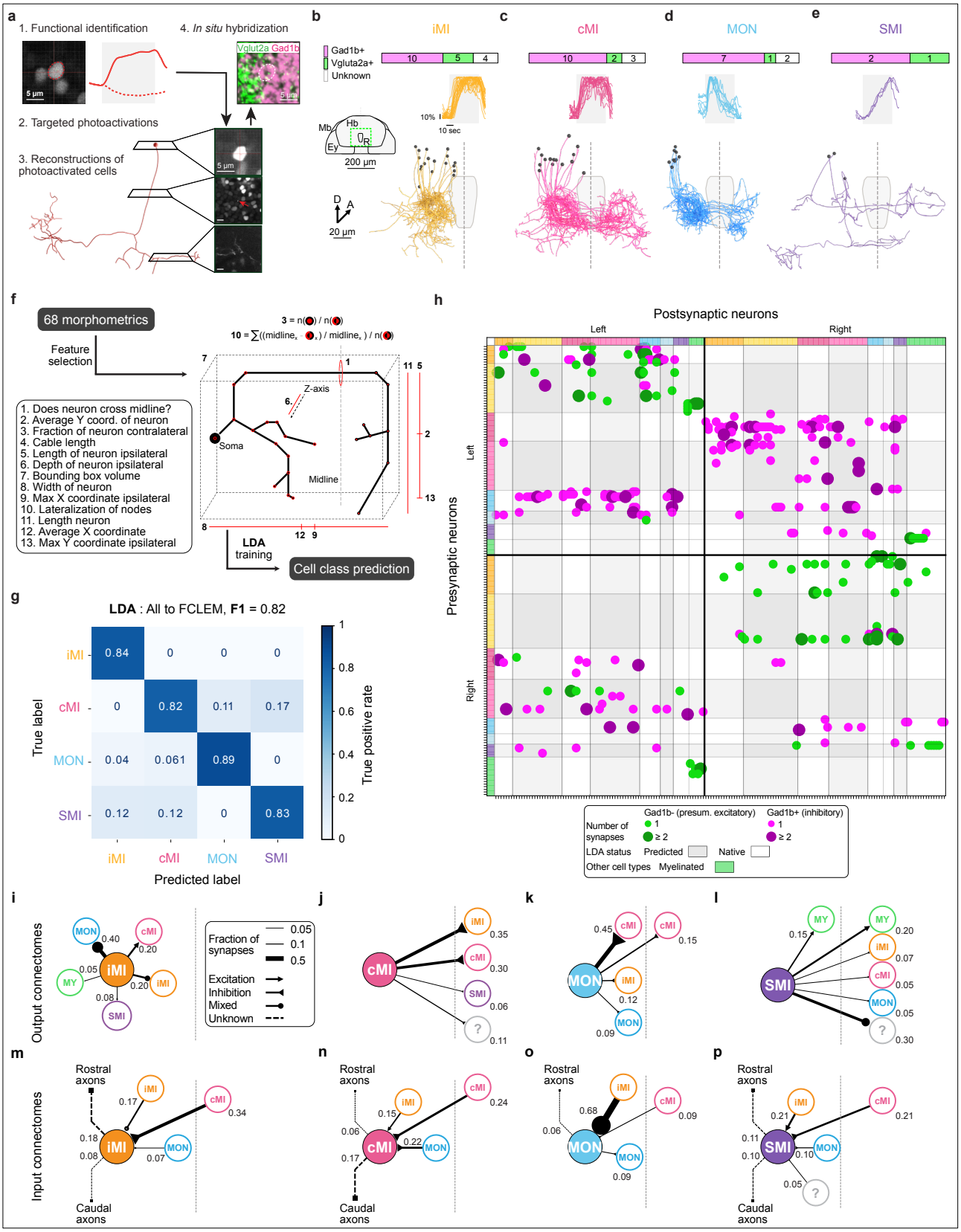

Fig. 3 | Single-cell photoactivation and functional type predictions across datasets. a, Schematic of the functional identification process followed by single-cell photoactivation, *in situ* hybridization, and manual morphological reconstruction. All scale bars correspond to 5 µm. **b,** Structure-function relationship of functionally imaged and photoactivated iMI neurons. Top: distribution of neurotransmitter identity shown as Gad1b-positive (black), Vglut2a-positive (gray), or unknown (white). Left: schematic showing coarse brain organization (coronal view) and location of the reconstructed neurons below (green dashed square) as well as surrounding outlines of the raphe. Right: traces representing the normalized $\Delta F/F_0$ neuronal activity over time. Bottom: reconstructed iMI neurons with somas in black. The dashed line represents the midline. Abbreviations: Mb, midbrain; Hb, hindbrain; R, raphe; Ey, eye; A, anterior; D, dorsal; V, ventral. **c–e,** identical representation for other neuron types. **f,** Schematic of the feature selection used for the linear discriminant analysis (LDA) to predict functional cell types. **g,** LDA confusion matrix of true positive rate using FCLEM and photoactivated neurons as the ground truth and predicting FCLEM cells. The prediction performance F1-score for the entire matrix is indicated in the plot title. **h,** Classifier-enhanced connectivity matrix of reconstructed EM neurons, sorted according to their functional types and hemispheres (thick black bars). The background of columns and rows of neurons whose functional type has been predicted through LDA is shaded in gray. Output (**i–l**) and input (**m–p**) cell-type connectomes extracted from the connectivity matrix. Connections accounting for less than 5% of the total synapse number are not shown. Question marks represent non-functionally imaged neurons that could not be classified by the LDA. The dashed line indicates the midline.

Structure-to-function classification

Our joint photoactivation and FCLEM datasets comprise a library of 131 cells (42 iMI, 44 cMI, 26 MON, and 19 SMI), establishing a direct link between structure, function, and neurotransmitter identity. This dataset can serve as ground truth for training a classifier. Using a linear discrimination analysis approach (LDA), we fitted a model that correlates morphological features with functional neuron type. LDA is a statistical method used for dimensionality reduction and classification, identifying a linear combination of features that optimally separates two or more classes by maximizing variance between classes while minimizing variance within classes. Analysis of the model parameter contribution (**Methods**) suggested that only a few metrics had strong predictive power (**Fig. 3f–g** and **Extended Data Fig. 6e**, **Methods**). Applying a cross-validation holdout strategy (**Methods**), we achieved a classifier predictive performance of 0.82 (F1-scores, **Fig. 3g**). This result indicates that our classifier can reliably predict the functional type of a neuron based solely on its morphology, even for cells it had not encountered during training. We further tested the classifier's performance with smaller datasets, using cells from either the photoactivation experiments or our FCLEM library. We still achieved predictive performance above 0.74 (F1-scores, **Extended Data Fig. 6f**). Remarkably, when training our classifier only on photoactivated cells and testing it on our FCLEM ground truth library, we maintained an F1-score of 0.76 (**Extended Data Fig. 6f**). These findings demonstrate that a classifier exclusively trained on light microscopy experiments can provide a generalizable, powerful, and cost-effective method for functionally labeling neurons in morphological libraries where functional imaging is absent, largely benefiting our current EM dataset, as well as other existing resources. We benchmarked our approach against other established methods (Li *et al.*, 2017; Choi, Kim and Hyeon, 2023) and found that our method consistently outperformed them in predictive accuracy (**Extended Data Fig. 6g–i**).

Enhancing the FCLEM dataset

A direct application of this approach is the enhancement of our correlated light and EM dataset. Within this dataset, we identified 108 pre- and postsynaptic reconstructed unmyelinated neurons that we had not functionally imaged during our initial two-photon session (**Fig. 2a**). Using our trained classifier, we predicted the functional types of 78.7% of the non-functionally imaged neurons, which considerably enriched our library with additional labels and allowed us to further populate the synaptic connectivity matrix of the anterior hindbrain (**Fig. 3h** and **Extended Data Fig. 7a–i**). Notably, the overall connectivity arrangements remained almost identical (**Fig. 3i–p**), confirming that our original dataset

contains a representative subset of functionally imaged cells. These results also indicate that our classifier can generate similar conclusions about the structure and function relationship of neural networks compared to what is achievable with FCLEM.

Morphological reconstructions and functional classification in a second whole-brain EM dataset

To test the generalizability of our classifier, we applied it to a second EM volume spanning the whole larval zebrafish brain (WBEM dataset, Petkova et al., co-submitted with this manuscript), including visual input regions absent from the FCLEM dataset (**Fig. 4a,b**). The WBEM dataset encompasses 800 × 450 × 250 µm from telencephalon to spinal cord and provides an ideal substrate for classifier-guided circuit reconstruction and long-range input reconstruction (**Fig. 4a–c**). Before EM processing, the specimen, expressing Gad1b+ and VGluT2a+ labels, was imaged by confocal microscopy, enabling later assignment of neurotransmitter identity via single-cell co-registration with the WBEM dataset (**Fig. 4b**).

We first reconstructed a random sample of 20 neurons from the anterior hindbrain (rhombomeres 1–3), of which 16 were classified as iMI, cMI, or SMI neurons. We focused on six iMI neurons as seed cells (four vGluT2a+, two unlabeled), given their central role in the integrator circuit (**Fig. 4c**). Tracing their 273 outputs revealed 159 postsynaptic neurons, of which 115 could be assigned a functional type using our classifier. The resulting inhibitory/excitatory ratios and functional type distribution closely matched those observed in the FCLEM dataset (**Figs. 4d–f** and **1f–i**). Analysis of iMI output connectomes revealed at least two distinct subpopulations: one displayed extensive recurrent connectivity with frequent polysynaptic motifs (**Fig. 4g,h)**, consistent with a role in evidence integration; the other included two seed neurons that projected selectively to the dorsal raphe (**Fig. 4i**), suggesting a dedicated pathway for neuromodulatory feedback (Kawashima *et al.*, 2016, 2024).

We next reconstructed all 273 inputs onto four recurrently connected iMI neurons, identifying 66 presynaptic neurons, of which 40 were assigned a functional type via our classifier. These inputs originated from two major sources: First, local inputs within the anterior hindbrain, consistent with recurrent excitation and bilateral inhibition motifs as found in our FCLEM dataset (**Figs. 4j** and **3m**). Second, we uncovered long-range excitatory ipsilateral inputs from multiple rostral brain regions. Surprisingly, most of the inputs arose from the thalamus with fewer contributions from the midbrain and pretectum (**Fig. 4j,k**). Many input neurons extended dendrites into retinal arborization fields, consistent with direct input from retinal ganglion cells (Kubo *et al.*, 2014b; Naumann *et al.*, 2016; Svara *et al.*, 2022). While earlier studies had pointed to the pretectum as the primary source of such inputs (Naumann *et al.*, 2016), our findings reveal a broader set of visual areas innervating integrator neurons. These results suggest that there may be wide-field direction-selective neurons in the thalamus. To probe this area for such activity, we performed two-photon calcium imaging targeting this and adjacent regions during random dot motion stimulation (**Extended Data Fig. 8b–c**). As expected, direction-selective responses were observed in the optic tectum and pretectum, but also in the thalamus. Moreover, the majority of WBEM input cells were located within 20 µm of a direction-selective neuron when mapped to a common reference brain (**Extended Data Fig. 8c**). Taken together, these results suggest that iMI neurons receive long-range, direction-selective inputs from the multiple visual processing regions, with the thalamus representing an unexpected and potentially important source.

Having established the long-range visual inputs to iMI neurons, we next asked whether MON cells might also receive direct synaptic input from early visual brain regions. We identified a MON-classified neuron in the anterior hindbrain and reconstructed all its presynaptic partners (**Fig. 4l,m**). We found a strikingly similar local input structure to that of functionally identified MON cells in the FCLEM dataset (**Fig. 3o**). In addition, one input neuron had its soma in the nucleus isthmi, an area

that had previously been attributed to visual stimulus selection (Henriques *et al.*, 2019). Taken together, these results confirm that MON neurons are targeted by local iMI neurons relaying whole-field visual flow from rostral visual areas.

In summary, this second EM dataset, despite lacking functional information, validates the use of morphology-based classifiers across datasets. Our approach provides a framework for dissecting sensorimotor integration in the zebrafish brain. Next, we set out to include these explicit and confirmed connectivity patterns, from both the WBEM and the FCLEM datasets, to constrain a realistic circuit model.

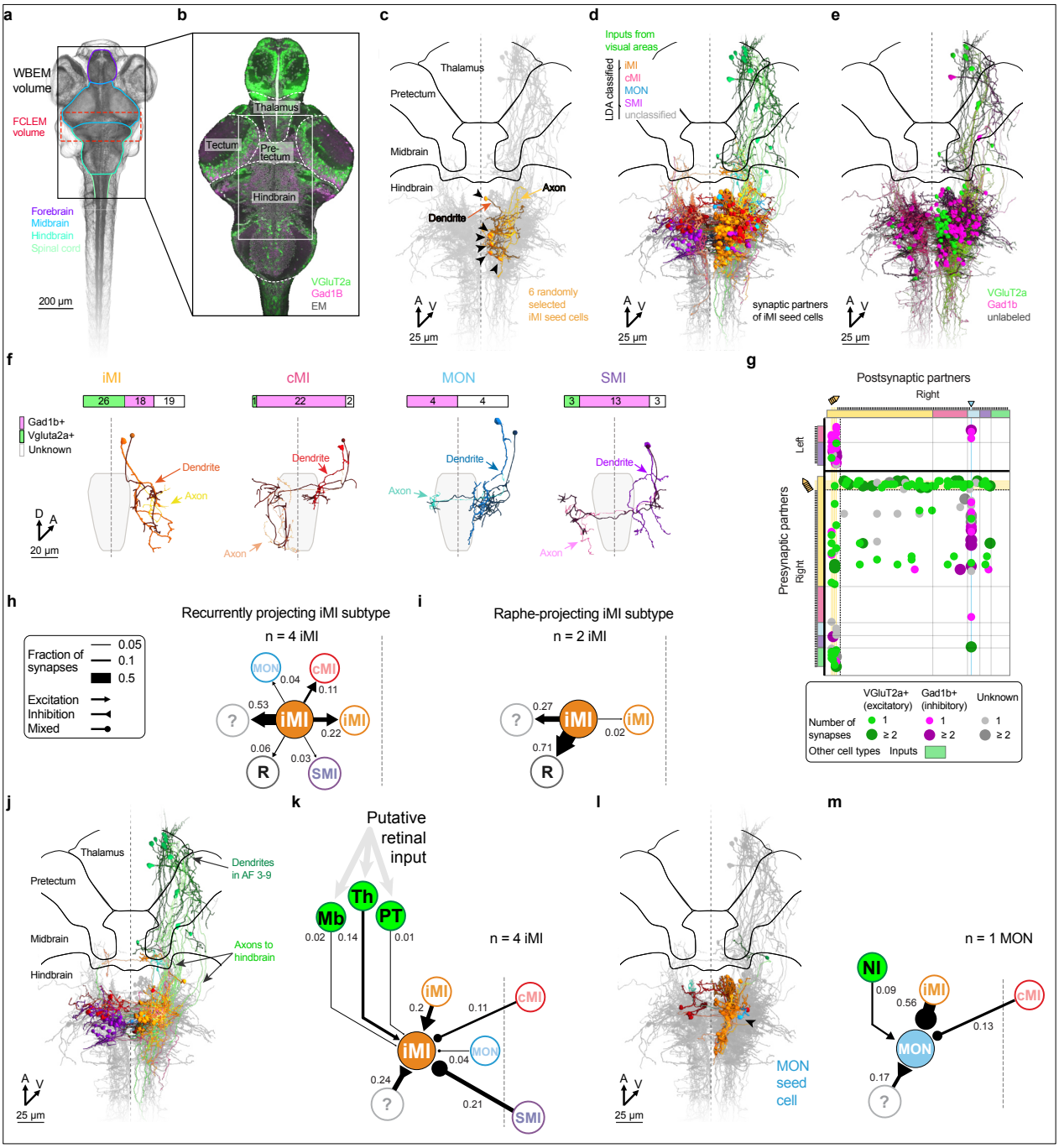

Figure 4 | Connectivity of hindbrain integrator circuit reconstructed based on LDA classification in a second EM dataset containing the whole larval zebrafish brain. a, WBEM and FCLEM volumes. The other regions were not imaged. **b,** Single EM plane in gray with registered confocal imaging. Magenta shows inhibitory neurons (Gad1b+). Green shows excitatory neurons (VGluT2a+). **c,** Six randomly selected neurons classified as iMI using our classifier (**Fig. 3f**). Arrowheads indicate somas. **d,** Presynaptic and postsynaptic partners of four recurrently projecting iMI neurons, colored by predicted morphotype. **e,** Dorsal view of 215 reconstructed forebrain and anterior hindbrain neurons, colored by neurotransmitter identity. **f,** Top: neurotransmitter identity of all functionally classified WBEM neurons. Bottom:

comparison between example photoactivated neurons from experiments in **Fig. 3a,b** and classified WBEM neurons. **g,** Connectivity matrix for LDA-classified WBEM neurons, organized by morphotype and hemisphere. Colored arrows and lines correspond to the connectomes shown in **h–m**. **h–i,** Output connectivity diagrams of six iMI neurons, separated into four recurrently projecting and two raphe-projecting subtypes (middle and left diagrams, respectively). All these neurons were considered excitatory. **j,** Presynaptic partners of four iMI neurons, showing long-range VGluT2+ inputs from the ipsilateral thalamus, midbrain, and pretectum. **k,** iMI connectome extracted from the connectivity matrix. **l,** Presynaptic inputs to a MON neuron. **m,** MON connectome extracted from the connectivity matrix. Abbreviations: Mb, midbrain; Th, thalamus; PT: pretectum; NI: nucleus isthmi.

An anatomically and functionally constrained circuit model of a flexible neural integrator

We had previously proposed a neural circuit arrangement of the anterior hindbrain, in which temporal integration of motion evidence may be implemented via recurrent connectivity of integrator cells (Bahl and Engert, 2020). These cells, we suggested, compete with a transiently active pool of inhibitory neurons, such that swimming is initiated when excitation overcomes inhibition. While in our previous model, we speculated about connectivity purely based on functional imaging from the soma, we now have detailed ground truth connectivity information: First, through the identified EM connections of functionally identified cells in our FCLEM dataset (**Figs. 2c–j** and **3i–p**) and, second, through the functionally classified cells in our WBEM dataset. To keep our new model tractable, we focused our analyses on the major contributors within the circuit that constituted at least 10 % of the input or output synapses. We also only considered identified connections between functionally labeled cells (**Figs. 2c–j** and **4h–m**). We assigned excitatory and inhibitory labels based on the observed majority of connection types within each cell type (**Figs. 1f–i**, **3b–e**, and **4e,f**). The resulting network connectivity matrix (**Fig. 5a**) allowed us to draw a putative circuit arrangement of the anterior hindbrain implementing the integration of visual motion cues and sensory-motor control (**Fig. 5b**). Key elements of this circuit arrangement are recurrent connectivity of excitatory iMI neurons (iMI^+), implementing the temporal filtering of signals, as well as delayed feedforward inhibition of MON cells via inhibitory iMI neurons (iMI^-). We also implemented a disinhibition motif by letting MON neurons inhibit inhibitory cMI cells as well as interhemispheric inhibition via cMI cells. iMI^+ and MON neurons compete for activating SMI cells, which in turn lead to activation of MY cells as a putative proxy of behavior. In our FCLEM dataset, we found several axonal segments coming from the anterior side of the brain, projecting onto iMI and MON cells (**Extended Data Fig. 7a**). The long-range tracing results in our WBEM volume further allowed us to add confidence to these projections (**Fig. 4e**). Based on these findings, we modeled inputs coming from the thalamus, midbrain, and pretectum regions onto iMI^+ and MON cells (**Fig. 4k,m**).

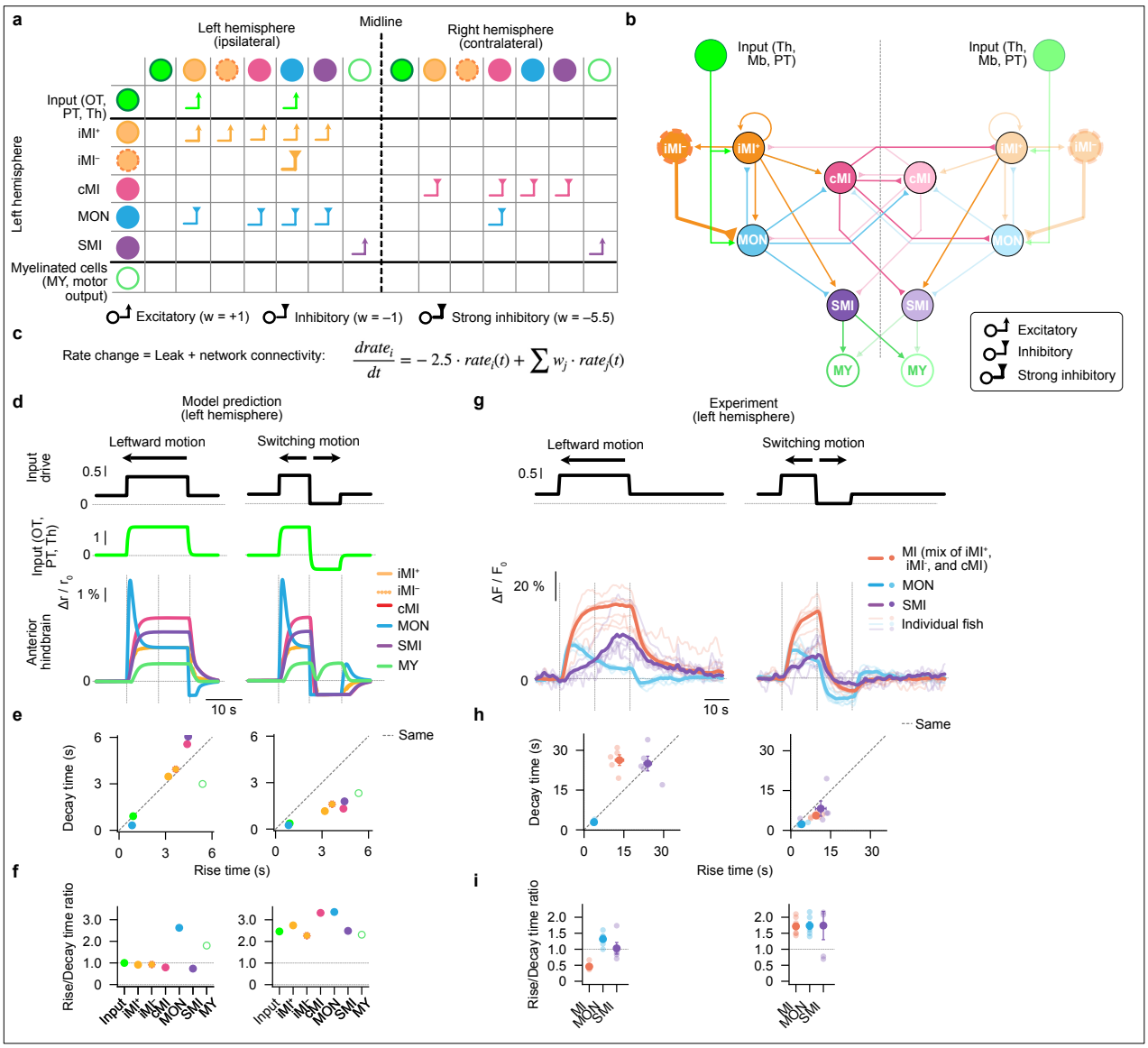

Fig. 5 | A connectome-constrained neural network model of the anterior hindbrain. a, Summary matrix of all identified connections with at least 10 % connectivity probability, based on our FCLEM and WBEM analyses. For simplicity, only connections originating on the left hemisphere are displayed. For neurons in the right hemisphere, the matrix is identical. Excitatory and inhibitory connections are indicated by arrowheads and triangles, respectively. **b,** Network model following the same connection scheme as in **(a)**. **c,** Differential equation for neuron *i*. The full model contains 14 units (7 on each hemisphere, **Methods**), following connectivity weights w_j shown in **(a)**, with equivalent leak factors (–2.5) across all cell types. **d,** Simulation results for two different stimulus configurations (leftward motion, left plot; switching motion, right plot). The input drive represents the stimulus direction on the left eye (positive for leftward motion, and slightly below baseline for rightward motion). Colored lines indicate the dynamics of units in the left hemisphere. Responses on the contralateral hemisphere are shown in **Extended Data Fig. 9a**. **e,** Rise and decay times (**Methods**) of cell types for different stimulus configurations. When the direction suddenly changes for the switching motion stimulus (right plot), integrator cells turn off more rapidly than if the motion just stops (left plot). **f**, Ratio of rise and decay times per cell type for the two stimulus configurations. Values of 1 (dashed line) mean that rise and decay times are similar (as seen for leftward motion, left plot). Larger values than 1 indicate that decay times are faster than rise times (as seen for switching motion, right plot). **g**, New two-photon imaging experiment following visual stimulation protocol in (**d**), showing response traces for each functional cell type (trial-, fish-, and cell-averaged). **h,i,** Same as in **(e,f)**, but for new experimental data. Decay dynamics of MI and SMI are faster for the switching motion stimulus (right plots) compared to when motion just stops (left plots). Thin lines and solid dots indicate individual fish (n=7 fish, 2 planes per fish, and 12 trials per plane).

In principle, the weight of all identified connections (= 144), the passive membrane biophysics, such as its leak constant (= 14), or even complex activity-dependent conductances and plasticity features

of each cell type, may be free model parameters and could be tuned to obtain the experimentally observed dynamics. We wanted to know to what extent a model behaves where these parameters are largely fixed. Given the observed equal distribution of synapse numbers and sizes (**Extended Data Fig. 4t,u**), we chose the same weights in the network across cell types (see **Methods** for parameter choice). Assuming all cells have the same membrane properties, we chose identical leak values across the network.

Model simulations revealed dynamics resembling the ones observed in experiments (compare **Fig. 5d**, left, with **Figs. 1f–i** and **3b–e**): For leftward motion, integrator cells in the left hindbrain had slower onset and offset dynamics than neurons in the simulated input regions. MON neurons showed their characteristic transient response at the start of motion. On the contralateral hemisphere, model integrator cells showed clear motion opponent inhibition, with MON neurons rebounding at stimulus offset, also matching experiments (compare **Extended Data Fig. 9a, Extended Data Fig. 1a, Extended Data Fig. 3c**, and (Bahl and Engert, 2020)). We further quantified the relationship between the rise and decay times of simulated neural activity for each cell type (**Fig. 5e**, left), revealing a mostly linear relationship, as expected from integrators with low-pass filter dynamics. To further quantify this relationship, we also computed the ratio between rise and decay times, which was around 1 for each unit but MON and MY. The good qualitative agreement between our network model and imaging data adds confidence that the proposed connectivity structure may indeed represent an important functional circuit motif in the anterior hindbrain.

After showing that we can match the known activity dynamics in the anterior hindbrain, we sought to further challenge and validate our model by explicitly testing some of its predictions on new functional imaging data. We presented the model with a stimulus in which motion direction abruptly changes from leftward to rightward motion—a configuration that we had not previously used when developing our experimental and modeling pipelines (**Fig. 5d**, right). Our model predicted a rapid activity state-switching across hemispheres upon direction change, with faster decay dynamics than if motion just stops (compare **Fig. 5e,f**, left, and right). We next probed these predictions via two-photon imaging (**Fig. 5g**). We presented larvae with the same stimuli as in our model and classified neurons based on the response dynamics to the stimulus continuously moving in one direction (same regressors as in **Fig. 1b**, **Methods**). The location of resulting cell types in the brain resembled the known distribution pattern (compare **Extended Data Fig. 9e** and **Fig. 1b**). Across stimuli, response dynamics in the experiment closely resembled model predictions. Quantification of the rise and decay times (**Fig. 5h,i**) showed that MI and SMI neurons turn off much faster for switching motion, compared to when motion just stops, hence also agreeing with our model predictions (**Fig. 5e,f**).

Based on our circuit model, we further argued that the inhibitory signal of the transiently active MON cells on the contralateral side (**Extended Data Fig. 9a**) at such transition points may be responsible for the observed dynamics. Its transient activation may rapidly release inhibition via cMI neurons, thus switching off the contralateral hemisphere. To test these ideas, we used our model to clamp the activity rates of MON neurons on both hemispheres to zero (**Extended Data Fig. 9b**). Such an experiment would be challenging to do in real larval brains, given the number and sparse distribution of MON cells. Model manipulation with silenced MON neurons predicted faster integration across the network. It also largely abolished the difference between onset and offset times (**Extended Data Fig. 9c,d**), suggesting that MON neurons indeed seem to mediate these dynamics.

Previously, we had proposed a minimal circuit arrangement of the anterior hindbrain, largely based on functional imaging only (Bahl and Engert, 2020). To quantitatively assess the performance of our old model, we implemented it in the same computational framework that we developed for our updated FCLEM / WBEM-constrained model (**Extended Data Fig. 9f,g**). For continuous leftward motion, our previous model captured neural dynamics across cell types (**Extended Data Fig. 9h**, left). This is expected, as we had previously designed the model to be able to do this. Our old model could also reproduce the relationship between rise and decay times (**Extended Data Fig. 9i,h**, left). However,

when displayed with the new switching motion stimulus, the rise and decay times were much closer to each other now (compare old model results in **Extended Data Fig. 9i,h**, right with the new model results in **Fig. 5e,f**). This discrepancy indicates that our previous model is less capable of capturing the rapid activity-state switching when visual motion cues abruptly change direction.

In summary, we find that our FCLEM / WBEM-constrained circuit model of the anterior brain can reproduce our experimentally observed dynamics of motion-sensitive cells in the anterior hindbrain. When motion direction abruptly changes, which is a realistic situation in natural environments, our model proposed that MON neurons allow the system to rapidly switch states, flexibly endowing the circuit with both slow integration capabilities and fast response times.

Discussion

Linking neural morphology with function has long been a major challenge in vertebrate connectomics, but recent advances have successfully achieved this by correlating functional imaging with electron microscopic circuit reconstruction in the mouse visual cortex (The MICrONS Consortium *et al.*, 2025) as well as in smaller circuits (Briggman, Helmstaedter and Denk, 2011; Lee *et al.*, 2016; Vishwanathan *et al.*, 2017; Bae *et al.*, 2018; Wanner and Friedrich, 2020; Svara *et al.*, 2022). In this study, we similarly combined functional calcium imaging with electron microscopy to uncover the circuit architecture underlying sensory evidence accumulation in the larval zebrafish anterior hindbrain, demonstrating the feasibility of this approach in a large, bilateral vertebrate brain network (**Fig. 1**).

Our findings provide the first mechanistic insights into how evidence accumulation of noisy visual motion cues is implemented within a recurrent neural network at the synaptic level. We identify interhemispheric inhibition and recurrent connectivity as key motifs of this circuit, a structure reminiscent of a line attractor (Seung, 1996; Khona and Fiete, 2022) (**Fig. 2**). Additionally, the presence of strong bilateral inhibitory interactions (including reciprocal inhibition), mediated by cMIs confirms previous predictions obtained in this region (Naumann *et al.*, 2016; Bahl and Engert, 2020) based solely on calcium imaging. These interactions were proposed to explain behavioral statistics of zebrafish larvae responding to whole-field motion. Reciprocal inhibitory connectivity has also been shown to underlie ring attractor networks encoding head direction in both vertebrates and invertebrates (Turner-Evans *et al.*, 2020; Petrucco *et al.*, 2023), raising the possibility that similar connectivity motifs contribute to sensory integration in the hindbrain. For example, cyclically connected populations of caudal hindbrain neurons contribute to persistent activity in neurons controlling horizontal eye movements (Vishwanathan *et al.*, 2024). While denser reconstructions may yet reveal such cyclic structures within the anterior hindbrain, our findings suggest that different motifs serve complementary roles in supporting persistent neuronal activity. Understanding how these motifs are specialized for their respective motor outputs will require further investigation. Our findings also complement earlier studies identifying rhombomere 1 of the hindbrain as an integrator of multiple sensory inputs such as luminance or gaze direction (Wolf *et al.*, 2017; Petrucco *et al.*, 2023). Whether the motion-sensitive neurons identified in this study may also integrate other sensory variables remains an open question.

We also demonstrate that MON neurons receive a mixture of excitatory and inhibitory inputs from two types of feed-forward connected iMI cells. Although the calcium dynamics were not sufficiently fast to disentangle the difference in onset time constant between these two populations, we propose that these neurons together provide first excitation and then delayed inhibition onto MONs, generating a transient activity pattern in these cells upon motion onset. A similar di-synaptic arrangement has been shown to generate fast, gated activity dynamics in the larval Xenopus visual system (Akerman and Cline, 2006). We also demonstrate that MON neurons provide strong ipsilateral inhibitory input to cMI neurons in an unexpected disinhibitory arrangement. Finally, our findings further support the

idea that SMI neurons act as the final readout of the evidence accumulation process, directly targeting reticulospinal neurons responsible for executing movement. The strong, stereotyped connectivity between SMI neurons and caudal-projecting reticulospinal neurons aligns with previous studies demonstrating that these neurons drive laterally biased motor outputs (Orger *et al.*, 2008).

Furthermore, we significantly expanded the utility of connectomic datasets by training and validating a classifier that predicts functional neuron types based solely on their anatomical features (**Fig. 3**), thereby allowing, in principle, functional inference in electron microscopy volumes where direct calcium imaging is not available. We directly tested the utility of this approach by applying our classifier to a second EM volume (**Fig. 4**). The classifier extracted functional cell types and circuit motifs that were remarkably similar to the ground truth established in the FCLEM dataset, and gave confidence that applying the LDA classifier approach to novel connectomics datasets has great potential for a community resource that allows linking structure to function. Using this approach, we uncovered that iMI neurons receive long-range excitatory input from the thalamus, conveying whole-field motion signals, suggesting a novel role for this region in sensory integration beyond its previously described function in conspecific recognition (Kappel *et al.*, 2022). Together, these findings provide strong support for the notion that functionally distinct neuronal populations exhibit conserved morphological features, at least within the anterior hindbrain of zebrafish. Future applications of this approach could extend to other brain regions and species, accelerating the functional annotation of large-scale connectomic datasets.

Finally, we incorporated our anatomical findings into a computational model of sensory integration, constrained by the observed connectivity patterns and neurotransmitter identities. By minimal tuning of connection weights and biophysical parameters, we demonstrated that our network model circuit could reproduce the experimentally observed dynamics of our measured cell types in the anterior hindbrain. The success of this model suggests an unexpected functional role of MON neurons in enabling fast responses to abrupt transitions in visual stimulation direction – a situation that frequently occurs in the naturalistic environment of animals (**Fig. 5**). The identified circuit arrangement in the anterior hindbrain may thus endow animals with a robust, yet flexible, system that can slowly filter important signals from noise and, at the same time, supports the rapid resetting of sensory integrators to allow fast reactions to external stimuli. Traditionally, disinhibitory connectivity in the motor system has been understood as a mechanism for movement initiation. Indeed, in the basal ganglia, disinhibition releases the thalamus and brainstem from suppression, allowing motor commands to propagate to the cortex and muscles (Lanciego, Luquin and Obeso, 2012).

It remains unclear how individual neurons' biophysical properties, as well as synaptic strengths, are shaping the dynamics observed in our analysis. For example, our model could not reproduce the observed slower ramping dynamics in SMI neurons, nor their trial-to-trial variability (Bahl and Engert, 2020). We also required the inhibitory inputs from iMIs to be increased to generate the correct MON neuron dynamics, potentially suggesting specific receptor types in these cells. Future experiments using voltage recordings, electrophysiology, transcriptomic analyses, and selective ablations could further refine our understanding of how such circuits are implemented. Recent analyses of *Drosophila* connectomes have integrated biophysical measurements to refine circuit models (Ammer *et al.*, 2023; Shiu *et al.*, 2024), an approach that remains largely unexplored in zebrafish. Measuring the biophysical properties of individual neuron types will be essential for further constraining network models and understanding the computational principles underlying sensory-motor transformations (Bargmann and Marder, 2013).

The connectomes and analysis tools presented here are openly available to the community and linked to an integrated atlas of the zebrafish brain. Our dataset provides a comprehensive view of vertebrate hindbrain circuitry in the zebrafish, complementing existing connectomic resources, including reconstructions spanning rhombomeres 4 to 8 (Vishwanathan *et al.*, 2024) of the ocular motor integrator system (Vishwanathan *et al.*, 2017), and whole-brain EM volumes (Svara *et al.*, 2022;

Petkova et al., co-submitted with this manuscript). Our light-microscopy-trainable classifier enables functional inference in electron microscopy volumes without requiring calcium imaging, providing a scalable, cost-effective approach for circuits tested across a wide range of experimental paradigms. Our strategy will accelerate high-throughput functional annotation of vertebrate brain networks, enabling further dissections of the computational principles underlying sensory-motor decision-making. More broadly, our findings lay the groundwork for applying connectomics to diverse neural circuits, bridging the gap between structure and function in the vertebrate brain.

Methods

Zebrafish

For the correlative light and EM experiment (FCLEM dataset, **Figs. 1** and **2**) we generated a triple transgenic *Tg(elavl3:H2B-GCaMP7f*$^{+/+}$*, gad1b:dsRed*$^{+/-}$ (Satou *et al.*, 2013)*, kdrl:mCherryCAAX*$^{+/-}$ (Fujita *et al.*, 2011)*)* larva obtained by crossing adult transgenic *Tg(elavl3:H2B-GCaMP7f, gad1b:DsRed)* and *Tg(elavl3:H2B-GCaMP7f, kdrl:mCherryCAAX)* lines in nacre background, *mitfa*$^{-/-}$ (Lister *et al.*, 1999) yielding high GCaMP7 fluorescence. The *Tg(elavl3:H2B-GCaMP7f)*^{u344Tg} transgenic line was generated using standard methods (Dowell *et al.*, 2024). We raised small groups of 20–30 larvae in filtered fish facility water in Petri dishes (9 cm in diameter) on a 14 h light, 10 h dark cycle at a constant 28 °C. From 4 dpf onwards, we fed larvae with paramecia once per day. The experiment was performed on 7-dpf larvae.

For sparse cell electroporations (**Extended Data Fig. 2a**), we incrossed *Tg(elavl3:H2B-GCaMP7f)*^{u344Tg} lines and selected offspring based on green fluorescence. For the area photoactivation (**Extended Data Fig. 2b**), we incrossed *Tg(alpha-tub:c3pa-GFP*$^{+/-}$*)*^{a7437Tg} (Bianco *et al.*, 2012) with *Tg(elavl3:H2B-GCaMP6s*$^{+/-}$*)*^{jf5Tg} (Freeman *et al.*, 2014) adults and selected offspring for green fluorescence. Animals were 7 dpf and 6 dpf old, respectively.

For the combined functional recordings, single-cell photoactivation, and HCR FISH staining experiments (**Fig. 3**), we outcrossed *Tg(alpha-tub:c3pa-GFP*$^{+/-}$*; elavl3:h2b-GCaMP6s*$^{+/-}$*)* and *Tg(alpha-tub:c3pa-GFP*$^{+/-}$*)*^{a7437Tg} adults, selecting for larvae that are homozygous for *c3pa-GFP* and heterozygous for *h2b-GCamp6s*.

For the imaging experiments in **Figs. 4** and **5**, we used incrossed *Tg(elavl3:GCaMP8s)*^{kn6Tg}, a newly generated line expressing *GCaMP8s* in neurons. To generate the line, we injected the Tol2 vector transgene construct (*Tol2-elavl3:GCaMP8s* (Zhang *et al.*, 2023)), obtained from Janelia Research Campus, and transposase RNA into 1–4-cell-stage embryos. We then isolated transgenic lines by screening for high expression of bright green fluorescence in the central nervous system in the next generation.

For the experiments shown in **Figs. 3**–**5**, larvae were raised in E3 water on a 14h light, 10 h dark cycle at a constant 28 °C without feeding. Animals were 5 dpf old.

All experiments were approved by the Harvard University and Konstanz University committees on the use of animals in research and training.

Visual stimuli

All visual stimuli during functional imaging consisted of ~1,000 dots (2 mm in diameter) moving at 1.8 cm s^{-1}, projected (60 Hz, P300 Pico Projector, AAXA) from below through mildly light-scattering parchment paper. Dots were shown in red on a black background to minimize interference of the visual stimulus with the functional GCaMP imaging. To ensure that the animals did not track individual dots to detect motion, each dot had a short lifetime (200 ms mean) and stochastically disappeared and immediately reappeared at a random location within the arena. One stimulation trial consisted of 40 s of 100% coherent motion either drifting leftward or rightward, interleaved by 20 s of 0% coherence

before and after. For the FCLEM experiment (**Fig. 1**), we also presented moving sine gratings drifting leftward or rightward, but did not include these stimulus trials in our analysis. For the imaging experiments in **Fig. 5g-i**, we presented animals with 30 s of 100 % coherence, with motion either running continuously or abruptly switching direction after 15 s. Stimuli across trials were interleaved with 40 s of 0% coherence. In all experiments, stimuli were shown in a random sequence.

Two-photon calcium imaging and analysis

For the FCLEM experiment, the larva was fully embedded in a drop of agarose (UltraPure Low Melting Point Agarose, Invitrogen), at ~35 °C in the center of a Petri dish (9 cm in diameter, VWR). After the agarose was solidified, the dish was filled with fish facility water and transferred into the measurement chamber of a custom-built two-photon microscope, operated by custom-written Python 3.7-based software (PyZebra2P). We used a femtosecond-pulsed laser (MaiTai Ti:Sapphire, Spectra-Physics) equipped with a set of x/y-galvanometers (Cambridge Technology), a 20x infrared-optimized objective (XLUMPLFLN, Olympus) to scan over the brain, and two photomultipliers (green and red) amplified by two current preamplifiers (SR570, Stanford) to collect fluorophore emissions. We used frame acquisition rates of around 1 Hz. Laser power was measured to be ~13 mW at the specimen. Such power levels did not interfere with behavior in previous tail-free imaging experiments (Bahl and Engert, 2020). During functional imaging, the laser was tuned to 950 nm to collect GCaMP7f fluorescence. We sequentially imaged six planes spaced at 12 µm, centered on the anterior hindbrain region (336 x 336 µm at 0.48 x 0.48 µm resolution). In each plane, we showed from 2 to 9 visual stimulation trials. Immediately after the experiment, we anesthetized the fish by replacing the water with a 0.015% MS-222 (Sigma-Aldrich) solution in fish facility water. This procedure enabled us to acquire an additional motion artifact-free high-resolution stack at 1020 nm excitation (420 x 420 x 90 µm at 0.6 x 0.6 x 2 µm resolution) with simultaneous collection of GCaMP7f and DsRed fluorescence. The total imaging session lasted ~5 hours.

Activity recordings of each plane were first motion-corrected using NoRMCorre (Pnevmatikakis and Giovannucci, 2017) and temporally averaged. We used a convolutional neural network segmentation approach (StarDist) to perform high-accuracy segmentation of the nuclei in each plane (Weigert and Schmidt, 2022). Calcium dynamics for each nucleus mask were then extracted as $\Delta F/F_0$ traces using Python numpy array slicing. K-means clustering of functional cell types was performed on pooled activity traces from the FCLEM experiment (**Fig. 1**) and all reconstructed neurons from our targeted photoactivations experiments (**Fig. 3**). The elbow method (Umargono, Suseno and S. K., 2019) suggested 4 functionally distinct clusters. These clusters were further isolated by two successive K-means clustering steps with 3 and 2 target clusters as parameters. The first iteration isolated MON dynamics, fast motion integrator dynamics (MI-1), and a third, slower group. The second iteration performed on this slower population revealed an additional motion integrator group (MI-2) as well as a slow motion integrator group (SMI). Thus, our clustering approach yielded 4 neuronal clusters with distinct temporal dynamics. For all cells in each cluster, we computed the average rise time until neuronal activity reaches 90% of the maximal response, revealing a clear separation of timescales across clusters (**Extended Data Fig. 1b**, only showing FCLEM cells). We then computed 3 final regressors by pooling neurons belonging to the MI-1 and MI-2 clusters and averaging the activity of all neurons belonging to each clustered population. Neurons in the FCLEM recording were then assigned to one of the 3 functional types by computing the correlation coefficient with individual regressors. Neurons whose correlation coefficient with a regressor was larger than 0.8 and that had a response of at least 20 % $\Delta F/F_0$ were assigned to the corresponding functional type. All other neurons remained unassigned.

Direction selectivity indexes (**Extended Data Fig. 1d**) were computed using standard methods (Boulanger-Weill *et al.*, 2017):

$$DSI = \frac{\max(R_R) - \max(R_L)}{\max(R_R) + \max(R_L)},$$

where $max(R_R)$ and $max(R_L)$ are the maximal $\Delta F/F_0$ response values during the entire rightward and leftward stimulation. Negative responses were set to 0.

For the imaging experiments presented in **Extended Data Fig. 8b,c** and **Fig. 5g–i,** we used our newly generated fish line *Tg(elavl3:GCaMP8s)^{kn6Tg}*. Raw imaging data was processed as previously described and neurons were segment using cellpose3 (Stringer and Pachitariu, 2025) on time-averaged imaging stacks, using the following cyto3 model parameters: cell diameter = none; follow threshold = 0.7; cellprob threshold = –0.4; lower = 0; upper = 90.0, which generated very good segmentation results across the brain (**Extended Data Fig. 8b** and **Extended Data Fig. 9e**). We computed $\Delta F/F_0$ time traces from the resulting masks.

In the imaging experiments presented in **Extended Data Fig. 8b–c**, individual neuron centroids were registered to the reference brain using ANTs (Avants, Tustison and Johnson, 2015; Randlett *et al.*, 2015). Next, we identified responsive cells by performing a one-sided t-test between the peak responses during stimulus and during pre-stimulus baseline lasting 10s for each cell. If either the left-motion or right-motion test had a p-value smaller than 0.005, we considered the cell responsive. We computed DSI as described previously and considered a cell as DS if its absolute DSI > 0.33.

In the imaging experiments presented in **Fig. 5g–i,** we used the same regressors and cell type classification strategy as for our other imaging experiments (**Figs. 1** and **3**). We then averaged all labeled cells per group to obtain response dynamics. For the continuous motion stimulus, we computed the time until neuronal activity reaches 90% of the maximal response during the time window of 30 s after motion onset. We chose the activity at the end of the stimulation period to compute the time until the activity decayed to 10 % of that value. For the switching motion stimulus, we used the 15 s time point as a reference using the same approach.

Sparse electroporations and area photoactivations

Sparse electroporations were performed as in (Boulanger-Weill *et al.*, 2017). Briefly, 4-dpf larvae were embedded in a droplet of agarose and anesthetized with 0.015% MS-222 (Sigma-Aldrich) in fish water. The agarose next to the anterior hindbrain was removed using a microsurgical blade. The electroporations were performed under a fixed-stage upright microscope equipped with a long working distance objective (10x UPlanFL N 10X/0.30na, Olympus). The silver wire microelectrode and bath electrode were mounted on micro-manipulators with the microelectrode holder containing an additional side port to apply air pressure with a syringe. Borosilicate glass capillaries (1.2 mm outer diameter, 0.68 mm inner diameter, with filament by World Precision Instruments) were pulled using a pipette puller (PC-10, Narishige, set at 68/58 °C) to obtain a 1 µm tip diameter. Pipettes were filled with 2 µL of *cmv:lyn-tdTomato* plasmid DNA solution and inserted into the anterior hindbrain of larvae. The lyn tag enables high-efficiency targeting of the red fluorescent protein to the cell's membrane and is thus ideal for studying neuronal morphology (Kunst *et al.*, 2019). Following optimized protocols (Zou, Friedrich and Bianco, 2016), two or three stimulation bursts (around 0.5 s per burst, consisting of 2 ms pulses at 200 Hz at 28 V were delivered using a square pulse stimulator (Sd9, Grass Technologies) and monitored using digital oscilloscope (TDS 2014, Tektronix). After the electroporations, larvae were freed from the agarose and kept isolated for 2 days. At 6 dpf, we then performed two-photon functional imaging of GCaMP6s (see previous section) to measure the response dynamics of the labeled cells to random dot motion. For subsequent morphological imaging of electroporated cells, we then anesthetized the fish and imaged at 1030 nm to collect dual-color z-stacks at high spatial resolution (0.46 x 0.46 x 1.5 µm) of both GCaMP and td-Tomato. Morphological imaging data was filtered (3D Gaussian blur, sigma 1.0 in x, y, and z) in Fiji (Schindelin *et al.*, 2012). Labeled neurons were then semi-automatically traced with the open-source reconstruction software neuTube (Feng, Zhao and Kim, 2015), using default settings and optimal node resampling. We then

saved cells as .swc files. Using the GCaMP6s channel, we then generated a transform per larva, allowing us to map reconstructed electroporated cells to a reference brain (Randlett, Wee, E. A. Naumann, *et al.*, 2015).

For area photoactivation (**Extended Data Fig. 2b**), fish were anesthetized with 0.015% MS-222 (Sigma-Aldrich), and c3pa-GFP was photoactivated using cycles of 40 short pulses of 200 ms at 1 Hz at a laser wavelength of 750 nm, following established protocols (Kramer *et al.*, 2019). After 1–3 initial trial pulses to check whether any adjacent cells were photoactivated and to readjust the region of interest if necessary, the whole protocol consisting of 15 cycles was executed, with five-minute intervals between two activation cycles. Photoactivation was targeted over a 50 x 40 µm region containing neurons with motion integration dynamics in the anterior hindbrain.

Sample preparation for the EM imaging

For the FCLEM experiment, we used a protocol modified from (Tapia *et al.*, 2012) to enhance extracellular space preservation, which improves synapse detection (Pallotto *et al.*, 2015) and permits single-cell resolution imaging using X-ray tomography. Unless noted, all steps were performed at room temperature (RT). Immediately after the two-photon stack acquisition, the larva was still anesthetized and embedded in agarose. We replaced the water with a dissection solution (64 mM NaCl, 2.9 mM KCl, 10 mM HEPES, 10 mM glucose, 164 mM sucrose, 1.2 mM $MgCl_2$, 2.1 mM $CaCl_2$, pH 7.5) supplemented with 0.02% tricaine (Hildebrand *et al.*, 2017). We then cut small slits in the agarose to expose the eyes and performed bilateral enucleations to enhance extracellular space preservation and heavy metal staining. We used a custom-made hook that was carefully inserted behind the eyes to prevent brain damage. The larva was immediately transferred to a fixation solution at 4°C (2.5% glutaraldehyde, 0.1M cacodylate buffer supplemented with 4.0% mannitol at pH 7.4). Cacodylate buffer: 0.3M sodium cacodylate, 6 mM CaCl2, pH 7.4. To improve the fixation, the tissue was rapidly microwaved (cat. no. 36700, Ted Pella, equipped with a power controller, steady-temperature water recirculator, and cold spot) in the fixative solution (this step lasted <5 min after initial transfer into fixative). The microwaving sequence was performed as in (Tapia *et al.*, 2012): at power level 1 (100 W) for 1 min on, 1 min off, 1 min on then to power level 3 (300 W) and fixed for 20 s on, 20 s off, 20 s on, three times in a row. Fixation was then continued overnight at 4°C in the same solution. The following day, the sample was then washed again in 0.5x cacodylate buffer (3 exchanges, 30 min each before osmication (2% OsO_4 in 0.5x cacodylate buffer, 90 min). After a quick wash (< 1 min) in 0.5x cacodylate buffer the sample was reduced in 2.5% potassium ferrocyanide in 0.5x cacodylate buffer for 90 min then washed with filtered H_2O (3 exchanges, 30 min each) and then incubated with 1% (w/v) thiocarbohydrazide (TCH) in filtered H_2O (and filtered with a 0.22 µm syringe filter before use) for 45 min to enhance staining (Hua et al., 2015). Due to poor dissolution of TCH in water, the solution was heated at 60 °C for ~90 min with occasional shaking before filtering and then placed at RT for 5 min before the incubation step. The sample was then washed with filtered H_2O (3 exchanges, 30 min each) before the second osmication (2% OsO_4 in filtered H_2O, 90 min) and then washed again (3 exchanges, 30 min each). Then, en-bloc staining was performed overnight using 1% uranyl acetate in filtered water at 4 °C. The solution was sonicated for 90 min and filtered with a 0.22 µm syringe filter before use. Steps involving uranyl acetate were performed in the dark. The following day, samples were then washed with filtered H2O (3 exchanges, 30 min each). Next, the samples were dehydrated in serial dilutions of ethanol (25%, 50%, 75%, 90%, 100%, 100% for 10 min each step) and then in propylene oxide (PO) (100%, 100%, 30 min, each step). Infiltration was performed using LX112 epoxy resin with BDMA (21212, Ladd) in serial PO dilution steps, each lasting 4h (25% resin/75% PO, 50% resin/50% PO, 75% resin/25% PO, 100% resin, 100% resin). Samples were mounted in fresh resin in a mouse brain support tissue (Hildebrand *et al.*, 2017) with the head exposed to facilitate cutting and prevent the sample from sinking to the bottom of the resin molds. Mouse tissue was fixed using standard procedures (Fang et al., 2018) and then cut into 2–3 mm wide cubes, which were pierced using a puncher (0.75 mm, 57395, EMS) to insert the larva. The cubes were stained

805 along with fish samples using the protocol described above, except that the uranyl acetate overnight
806 step was performed at RT. The samples were then cured with support tissue for 3 days at 60 °C. For
807 all steps, a rotator was used. Aqueous solutions were prepared with water passed through a
808 purification system (Arium 611VF, Sartorius Stedim Biotech). The protocol lasted 5 consecutive days,
809 including surgery, fixation, staining, and resin embedding, followed by 3 days of resin curing.

810 **X-ray computed tomography**

811 To achieve high contrast X-ray and mSEM imaging, we sequentially optimized OsO_4 staining duration,
812 X-ray imaging, and voltage, and performed deep learning-based X-ray reconstruction (**Extended**
813 **Data Fig. 2e,f**). The OsO_4 staining was optimized first in previous batches of samples to yield the
814 mSEM staining protocol described previously. The imaging voltage and post-processing were
815 optimized in the main sample described in this study. In total, this sample was imaged for ~300 hours,
816 which did not interfere with mSEM imaging. For each sample, the block was trimmed to expose the
817 head of the fish for imaging (Xradia 520 Versa, ZEISS). To assess the imaging quality, we computed
818 a modified version of Michelson's contrast that was robust to noise at multiple sections along the main
819 axis of the larvae:

820 $$\mathrm{Contrast} = \frac{I_{\max} - I_{\min}}{I_{\max} + I_{\min}}$$

821 Where I_{max} and I_{min} are the average intensity values over the 80th and below the 20th percentile,
822 respectively. We also computed the signal-to-noise ratio (SNR) at the same locations according to
823 (Joy, 2002). X-ray tomography stacks were post-processed using a deep neural network product
824 included in the Xradia software.

825 **Sample sectioning and mSEM image acquisition**

826 After X-ray imaging, the block was re-embedded in resin and cured for 3 days at 60 °C and trimmed
827 into a diamond shape (Hildebrand *et al.*, 2017). 4010 sections ranging from 30 to 35 nm were
828 automatically collected on carbon-coated tape using a custom tape collection device (ATUM)
829 (Hayworth *et al.*, 2014) mounted to a commercial ultramicrotome. The tape was cut into strips and
830 deposited on 30 silicon wafers that were post-stained (Hildebrand *et al.*, 2017). Wafers were then
831 mounted on the 61-beam mSEM stage (MultiSEM 505, ZEISS), and each section's position was
832 determined using a reflected light microscope to guide the high-resolution imaging. Imaging was
833 performed at 4 x 4 nm pixel resolution using secondary electron emission using a dwell time of 400
834 ns per pixel. The quality of each section was assessed using previously described methods (Shapson-
835 Coe *et al.*, 2024).

836 **mSEM image alignment, stitching, rendering, neuronal morphology proofreading**

837 We trained convolutional neural networks to detect defects and classify locations that contain tissue
838 for each montaged section. We used self-supervised convolutional neural networks to generate dense
839 displacement fields between sections (Popovych *et al.*, 2024), and then hierarchically minimized the
840 elastic energy in the set of all displacement fields to produce an aligned image. We created an "image
841 mask" that contained defects and locations that were classified as misaligned. We trained
842 convolutional neural networks that we used to segment cells, detect synaptic clefts, compute their
843 sizes, and assign presynaptic and postsynaptic objects from the cell segmentation at each cleft
844 (Macrina *et al.*, 2021). Cell segmentation and synapse detection and assignment used the aligned
845 image with locations in the "image mask" set to black. We refined the detection of synaptic clefts and
846 reduced false positives by visually inspecting two dendrites and one axon and classified predicted
847 synapses as true positive, false positive, and identified false negative missing synapses (**Extended**
848 **Data Fig. 4b–d**). We performed a Receiver Operating Characteristic (ROC) curve analysis to
849 establish a size threshold that minimizes false positives (**Extended Data Fig. 4e**). This analysis
850 determined that a synapse size threshold of 44 voxels effectively excluded 90% of the false positive
851 synapses, providing a reliable criterion for refining the dataset and improving prediction accuracy.

852 Finally, cell segmentation was ingested into the ChunkedGraph proofreading system so that
853 morphological errors could be manually corrected, and synapses were ingested into an annotation
854 table for consistent analysis (Dorkenwald *et al.*, 2023).

855 **Multimodal, reference brain registrations and cell type determination**

856 Matching of neuronal identities from the 2P functionally imaged planes to the EM volume was
857 performed in two successive manual steps using the Fiji plugin Bigwarp (Bogovic *et al.*, 2016). We
858 first manually registered functional imaging planes to a higher z-resolution two-photon image stack
859 (z-steps = 2 µm, containing green and red fluorescence) using manually selected 844 landmarks. The
860 SNR of this stack was enhanced using content-aware image restoration (Weigert *et al.*, 2018). We
861 then registered this higher resolution two-photon image stack to a downsampled mSEM stack (0.512,
862 0.512, 0.480 µm/pixel) using manually selected 771 landmarks. This EM stack was downloaded from
863 Neuroglancer (https://github.com/google/neuroglancer) using Cloudvolume (Silversmith *et al.*, 2022).
864 These two registration steps generated two deformation fields which were successively applied to the
865 2P functionally imaged planes using Bigwarp (in linear deformation mode) and manually checked
866 exhaustively. The segmented neuronal masks were also deformed using these two steps (in nearest
867 neighbor mode). Deformed planes of green and red fluorescence (8-bit image stacks) and segmented
868 masks were uploaded to Neuroglancer using Cloudvolume, enabling collaborative reconstruction and
869 cell type determination of the neurons of interest. To determine whether neurons were inhibitory, we
870 manually traced a mask surrounding the neurons' nuclei in the green channel and computed the
871 average corresponding red fluorescence. Neurons with values superior to 10 % of the maximum red
872 signal (25 on an 8-bit scale) were considered inhibitory. Regions containing k-means clustered
873 neurons (**Extended Data Fig. 1c**) were determined by automatically registering the 2P functionally
874 imaged planes to the z-brain reference brain (Randlett, Wee, E. A. Naumann, *et al.*, 2015) using ANTs
875 (Avants, Tustison and Johnson, 2015). For regional annotations, we downloaded anatomical masks
876 from the mapZebrain atlas platform (Kunst *et al.*, 2019) and mapped them into the z-brain coordinate
877 system (Randlett, Wee, E. A. Naumann, *et al.*, 2015) using ANTs (Avants, Tustison and Johnson,
878 2015).

879 Finally, neurons traced in Neuroglancer were downloaded using Navis (Schlegel *et al.*, 2025) and
880 automatically registered to the z-brain reference brain (Randlett, Wee, E. A. Naumann, *et al.*, 2015).
881 To register cells from our downsampled mSEM stack to the z-brain reference brain, we manually
882 selected 207 landmarks in the mSEM stack and the *Tg(elavl3:H2B-RFP)* confocal stack in the z-brain
883 coordinate system to generate a bridge transform via Fiji Bigwarp. All neurons presented in this paper
884 have been registered to the z-brain reference brain (Randlett, Wee, E. A. Naumann, *et al.*, 2015) and
885 are available on our online platform.

886 **Two-photon photoactivation and neurotransmitter identity of functionally identified cells**

887 We selected larvae for green fluorescent nuclear expression and embedded animals in a droplet of
888 low-melting point agarose in a Petri dish with a diameter of 6 cm. The fluorescence of the H2B-
889 GCaMP6s makes the identification of c3pa-GFP difficult – at this stage, c3pa-GFP is not yet
890 photoactivated and thus very dim. To enable screening for c3pa-GFP, we initially performed a brief
891 activation experiment in the two-photon microscope, labeling a small region in the dorsal rostral
892 tectum. We only continued with the animals that showed some sign of tectal photoactivation patterns
893 after a maximum of 5 rounds of photoactivation. Morphologies originating from this area largely
894 remained local and did not overlap with the photoactivated neurons in the hindbrain. In a few cases,
895 neurons descended into the anterior hindbrain neuropil, coming close to the photoactivated cells, but
896 did not interfere with our tracing. To accommodate larvae to the experiment and minimize motion
897 artifacts and plane shifts during imaging, we initially presented animals for 15 minutes with random
898 dot motion before starting the functional characterizations.

To quickly identify cell types, we then imaged a single plane in the anterior hindbrain for 15 – 30 minutes while presenting random dot motion. Using a custom-written Python script, we aligned recordings to the onset of motion and averaged stacks across trials. Using Fiji (Schindelin et al., 2012), we defined a small movable region of interest with the size of a cell to manually explore the stack for neuronal dynamics matching the known cell type dynamics (Bahl and Engert, 2020). This analysis step took less than 5 minutes per fish.

For each identified cell, we then conducted targeted photoactivation at 760 nm. Using a custom-written scanning waveform generator in PyZebra2P, we used a small activation spiral (less than 0.5 µm in diameter), focused onto the center of the nucleus of the cell. Due to the point spread function of our microscope (~1 µm along the horizontal plane, and ~4 µm along the vertical axis), we were able to activate c3pa-GFP in the cytosol without affecting neighboring neurons. Following recent protocols (Kramer *et al.*, 2019), we used short activation pulses of 200 ms in length and 100 ms interpulse intervals. The required laser power at the specimen and the pulse counts for effective photoactivation varied widely across fish. Some fish only required as few as 20 pulses (ca. 6 seconds) at 5 mW to activate cells, whereas other fish often required up to 1000 pulses (ca. 5 min) at 8 mW. We attribute this difference to variations in expression levels, as some experimental fish are heterozygous and some fish are homozygous for c3pa-GFP.

Following successful photoactivation, we anesthetized the fish by replacing the water in the Petri dish with a 0.015% MS-222 solution. After 15 minutes of anesthesia, we then imaged a high-resolution stack (100 planes, 0.4 µm x 0.4 µm x 2 µm; 90 s per plane) of the hindbrain and midbrain to capture as much of the photoactivated cell's neurite morphology as possible. This step took around 2.5 hours per animal.

To determine the neurotransmitter identity of the labeled cell, we performed HCR RNA-FISH (Choi *et al.*, 2018) on the same fish immediately after the imaging session. To this end, we cut out a small block of agarose containing the anesthetized fish and directly fixed the sample in ice-cold 4% PFA for 12–16 hours overnight at 4 °C. We then followed recent protocols optimized for zebrafish larvae (Shainer *et al.*, 2023). We used probe sets against *gad1b* (probe set size 30, #NM_194419.1) and *vglut2a* (*slc17a6b*, probe set size 20 #NM_001128821), with B1 and B2 amplifiers, respectively. We used the B1-546 amplifier fluorophore and the B2-405 amplifier fluorophore, thus fluorescently labeling *gad1b*-positive cells in red and *vglut2a*-positive cells in blue.

After the procedure, we placed the still agarose-embedded fish into the same two-photon microscope where it had been imaged before. The PFA fixation and HCR RNA-FISH protocol considerably reduced the fluorescence of a photoactivated c3pa-GFP cell. Cells were still identifiable because they were slightly more fluorescent than neighboring non-photoactivated neurons. Neurites in the photoactivated cells were, however, not visible anymore after the procedure. To further validate the identity of the cell, we used landmarks such as the arrangement of neighboring nuclei or neuropil structures with distinguishable distances to the labeled cells. We acquired two separate high-resolution volume scans around the photoactivated cell body. Our custom-built microscope can only simultaneously image green and red fluorescence or green and blue fluorescence, with a manual replacement of a filter cube in the collection optics path between imaging sessions. As we acquired green fluorescence in both sessions, we could identify our target cells in both imaging stacks to extract the expression levels of both *gad1b* and *vglut2a* within the cytosolic ring around the nucleus. Labels were largely exclusive to each other, allowing us to confidently assign neurotransmitter identity based on which label was stronger. We labeled cells where both *gad1b* and *vglut2a* signals were indistinguishable from background fluorescence as 'undefined'.

The custom-designed two-photon microscope used for these experiments was largely similar to the one explained above, used for the FCLEM experiment. However, this system used a tunable MaiTai ® DeepSee (Spectra-Physics) laser source with a built-in pre-chirp unit, a Nikon 25x Objective (N25X-APO-MP), and a more sensitive Hamamatsu GaAsP PMT (H16201P-40-S3) for the green

channel. These features significantly improved the imaging quality of green signals and later facilitated the reconstruction of photoactivated neurons. Reconstructions were performed in Fiji using the SNT semi-automated tracing tool (Arshadi *et al.*, 2021).

Zebrafish-optimized NBLAST probability matrix

We used NBLAST (Costa *et al.*, 2016) to compute a matrix of morphological similarity of cells within our FCLEM dataset (**Extended Data Fig. 3e–f**). One of the major functions of the NBLAST algorithm is the 2-dimensional scoring matrix (10 x 21), which provides a raw score of whether two neurons belong to a similar cell type. The row of the scoring matrix represents the dot product of the tangent vectors, whereas the columns represent the range of distances in micrometers. The default matrix is derived from a dataset of *Drosophila* neurons and is sensitive to several factors, including dataset type, neuron size, preprocessing methods, and the volume analyzed. To match the algorithm to our data, we computed a zebrafish-optimized scoring matrix using the FCLEM dataset. The training of such a matrix requires matching and nonmatching sets of neurons (Costa *et al.*, 2016). We used our four functionally and morphologically distinct cell types (iMI, cMI, MON, SMI) as matching sets. Non-matching sets of neurons are drawn randomly from our FCLEM dataset. The consistency of the matrix is assured by using the n-fold (n=4). The detailed method and further advancements are provided in an upcoming atlas paper (Vohra et al., *in preparation*).

Morphology-based prediction of neuronal functional types

With the unique availability of two ground truth datasets of structure and function relationship (**Fig. 1** and **Fig. 3**), we sought to employ and train a classifier to predict a functional cell type based on anatomical structure. Such a classifier will be useful for predicting functional response properties of cells in anatomical libraries for which functional imaging has not been performed, including existing EM reconstruction databases. To this end, first mapped all reconstructed neurons to a common reference atlas (Randlett, Wee, E. a Naumann, *et al.*, 2015), using custom-written Python scripts and ANTs (Avants, Tustison and Johnson, 2015). For neurons originating from the FCLEM experiment (**Fig. 1**), we applied the same Bigwarp-based generated ANTs transforms that we used to map cell bodies into the reference brain (see section above). For neurons originating from the two-photon guided photoactivation experiments (**Fig. 3**), we used the h2b-GCaMP6s channel to generate a transform between each stack against the corresponding reference stack.

Reconstructed neurons from the FCLEM experiment were downloaded as high-resolution geometry (.obj) files. These files are simple text files containing a list of surface vectors describing volumetric meshes, allowing us to apply our ANTs transforms to map geometries into the z-brain coordinate system. Using the *skeletor* package and the TEASAR algorithm (Sato *et al.*, 2000) in Python, we skeletonized .obj files to 1.5 µm spacing and saved results as .swc files. This procedure ensured that all neurons originating from different experiments and modalities ended up in the same coordinate system with the same spatial tracing resolution, a prerequisite for the development of our classifier.

As our NBLAST matrix does not show a clear separability of cell types, we decided to build our classifier using a feature-based approach. To this end, we exhaustively extracted 68 morphometrics from each skeletonized neuron (**Extended Data Table 1**). All features were normalized by subtracting the mean and scaling to unit variance across cells. To identify the most relevant of these features for predicting functional cell types, we first selected feature subsets of different sizes. To this end, we conducted feature ranking with reverse feature elimination using *sklearn.feature_selection.RFE* in Python with “AdaBoostClassifier” as the learning estimator. For a given target feature subset size (1 – 68), the algorithm starts at the maximum number of features (68). It then uses the specified estimator to evaluate the importance of features by fitting the model and then iteratively removing the least significant feature until it reaches the desired target feature subset size. For each resulting feature subset, we then extracted a predictive F1-score of how these features could be used to classify

cell types. Specifically, we split our cells (including both data from the FCLEM and photoactivation experiments) in a ratio of 70% train and 30% test. As a classifier algorithm, we chose Linear Discriminant Analysis (LDA) with solver 'lsqr' (least squares solution). Performing the LDA training and prediction step 100 times with different randomly selected training and test sets, allowed us to compute the predictive F1-score as a function of the feature subset size (**Extended Data Fig. 6e)**. We then selected the feature combination with the highest predictive performance as the final feature set (**Fig. 3f**). We used this feature subset for all further cell type classifications.

Many cells identified through our pre- and post-synaptic connectomic reconstructions had their soma in regions that were not covered by our 2P multi-plane imaging session. To compute the performance of our classifier when predicting the functional type in such cases, we performed a 'leave-one-out-cross-validation' step on our ground truth datasets. To assess the quality of the classifier using maximal and cross-modality training data, we combined both the FCLEM and photoactivation experiments. We iteratively chose one of our known FCLEM cells and trained our classifier on all remaining ground truth cells. Comparing the classifier prediction of the left-out FCLEM cell with its true functional type allowed us to compute a confusion matrix, indicating the probability that a functional prediction of a given FCLEM cell is correct (**Fig. 3g**). We finally repeated the training on all available ground truth cells (data from the FCLEM and photoactivation experiments) to generate the final classifier used to predict the functional type of FCLEM and WBEM cells that were not functionally imaged (**Figs. 3h, 4c–d**). Our trained cell type classifier should also be applicable to enhance other morphological resources, containing anatomical reconstructions of neurons in the larval zebrafish anterior hindbrain.

Notably, the LDA classifier will place any target cell, even when it looks completely different from the training dataset, into one of our defined 4 categories. To rule out such incorrect predictions, we identified outliers within the predicted cells' morphometric features using an isolation forest algorithm (*sklearn.IsolationForest*) and the local outlier factor (*sklearn.LocalOutlierFactor*). We trained these outlier removal methods with the morphometric features of our functionally identified cells from both the FCLEM and photoactivation experiments.

We finally compared our morphology-based neuronal type prediction method to previously established approaches (Li *et al.*, 2017). To do so, we computed persistence vectors and their sampled versions (Li *et al.*, 2017) for each neuron using *navis.persistence_vectors* and trained a linear discriminant analysis classifier (*sklearn.LinearDiscriminantAnalysis*) to predict functional types (**Extended Data Fig. 6g,h**). Similarly, we calculated form factors (Choi, Kim and Hyeon, 2023) for each neuron using *navis.form_factor* and trained another linear discriminant analysis classifier to predict functional types (**Extended Data Fig. 6i**).

Neuron reconstructions in the WBEM dataset

To obtain high-quality, exhaustive reconstructions in the WBEM dataset, each neuron was reconstructed independently by at least two expert proofreaders using automatic segmentation algorithms in Neuroglancer. To minimize anatomical bias for selecting seed cells, we generated a list of IDs containing all automatically extracted cell bodies in the integrator region of the anterior hindbrain (containing rhombomeres 1-3) and randomly shuffled this list. We then attempted to completely reconstruct the axons and dendrites of each neuron in the shuffled list in chronological order. Only neurons whose axons and dendrites terminated in natural endings within the volume (i.e., in arborizations or synaptic boutons) were deemed to be complete and were included as seed cells. Whenever tracing of axons or dendrites could not be continued due to issues with tissue quality, a neuron was discarded as a seed cell. After we had reached the predetermined number of 20 seed cells, we turned to the synaptic partner reconstructions. This very stringent quality criterion was slightly relaxed for the synaptic partner reconstructions because we had to optimize the level of completeness of reconstructions with the number of neurons that could be included in the dataset. Here, all neurons were included that could be reconstructed by at least two proofreaders

1045 independently to a 'completeness' of ~80%, when compared with the seed cells. This level of
1046 completeness proved to be sufficient for excellent LDA classification results. Neurons that passed
1047 these criteria were then added to the database of reconstructed morphologies and assigned a
1048 functional type by the LDA classifier, as described above.

1049 **Neurotransmitter assignment in the WBEM dataset**

1050 Each reconstructed neuron was assigned a neurotransmitter label in a blinded manner with respect
1051 to its morphology and functional morphotype assignment. To that end, we manually inspected the co-
1052 registered EM and confocal volumes. A neurotransmitter was only assigned when clear landmarks
1053 were present in both imaging modalities, i.e., blood vessels, ventricles, the midline, other anatomical
1054 structures, or constellations of neighboring cell bodies that could be co-referenced unambiguously.
1055 When an EM cell body could not be unambiguously identified in the confocal volume, the
1056 neurotransmitter was recorded as 'unclear'. In some cases, an individual EM cell could not be
1057 identified in the confocal volume because it was located in a densely labeled population of, e.g.,
1058 Gad1b+ neurons. In such cases, the cell was labeled as Gad1b+. Across the dataset, 101 neurons
1059 were labeled as Vglut2a+, 161 neurons were labeled 'Gad1b+', 25 neurons were labeled as 'unclear',
1060 and 44 neurons were labeled as 'unlabeled'. In the latter case, a clear cross-referencing of the cell
1061 body was possible, but the same cell contained no Vglut2a or Gad1b label in the confocal volume.

1062 **Synapse detection and synaptic partner reconstructions in the WBEM dataset**

1063 At the onset of the project, automatic synapse detection was not yet available in the WBEM dataset.
1064 Therefore, we opted for a completely manual synapse detection approach. Because manual synapse
1065 detection is generally considered to be ground-truth data and is used to benchmark automated
1066 synapse detection algorithms, we opted to continue using manual synapse detection even after
1067 automated detection became available. As with the neuron reconstructions, the dendrites and axons
1068 of every iMI seed cell were searched by at least two expert proofreaders for synaptic specializations
1069 and a consensus list of synapses was generated. Then, we attempted to reconstruct the synaptic
1070 partner of the synapse of interest to its parent cell body. Our success rate for reconstructing dendrites
1071 of postsynaptic neurons was 72%, while the success rate for tracing the axons of presynaptic partners
1072 back to a parent cell body was 24%.

1073 **Network modeling**

1074 We simulated the network model of the anterior hindbrain via an array of 14 first-order coupled
1075 differential equations (7 cell types on each hemisphere). We fed stimulus input drives into the first
1076 processing layer (input; optic tectum, pretectum, and thalamus) on the left and right sides,
1077 respectively. Input drives had a baseline activity of 0.5. A stimulation level of 100% random dot motion
1078 coherence to the left was simulated as increasing the input drive on the left by +1, and reducing it by
1079 0.5 on the right side (**Fig. 5d**). For motion to the right, the input drive was adjusted accordingly. We
1080 did not attempt to build a biophysically realistic network model of the pretectum or other midbrain
1081 regions (Kubo *et al.*, 2014a; Naumann *et al.*, 2016; Wang *et al.*, 2019). The activity was then further
1082 processed in the interhemispheric anterior hindbrain network. To keep the model simple and
1083 parameter space low, we fixed excitatory weights to +1 and inhibitory weights to –1. Because we
1084 found the connection between iMI^{-} and MON to be prominent in our data (**Figs. 3o** and **4m**), we here
1085 used a stronger inhibitory weight of –5.5. We modeled all cells with the same leak factor of –2.5,
1086 without assuming any specific biophysical features across the network. (**Fig. 5c**). Smaller leak factors
1087 than this value led to unstable network behaviors. Larger leak values led to overall faster dynamics.
1088 As our experimental measurement relies on cytosolic GCaMP8s calcium imaging (**Fig. 5g–i**), which
1089 represents a low-pass filtered version of the true neuronal activity, we did not aim to quantitatively
1090 match the time scales between model and experiment. The self-recurrency of iMI neurons effectively
1091 reduced the leak of this cell type, explaining the slower integration dynamics compared to input
1092 signals. Other neurons in the network model inherit these dynamics, explaining the overall slower

temporal dynamics in the hindbrain. We used the Euler method (time step dt = 0.01 s). The full model follows these rules to update the firing rates:

Left hemisphere:

$$
\begin{aligned}
d\mathrm{I}_l^+ &= -2.5 \cdot \mathrm{I}_l^+ + \mathrm{Stim}_l(t) \\
d\mathrm{iMI}_l^+ &= -2.5 \cdot \mathrm{iMI}_l^+ + 1.0 \cdot \mathrm{I}_l^+ + 1.0 \cdot \mathrm{iMI}_l^+ - 1.0 \cdot \mathrm{MON}_l^- - 1.0 \cdot \mathrm{CMI}_r^- \\
d\mathrm{iMI}_l^- &= -2.5 \cdot \mathrm{iMI}_l^- + 1.0 \cdot \mathrm{iMI}_l^+ \\
d\mathrm{CMI}_l^- &= -2.5 \cdot \mathrm{CMI}_l^- + 1.0 \cdot \mathrm{iMI}_l^+ - 1.0 \cdot \mathrm{MON}_l^- - 1.0 \cdot \mathrm{CMI}_r^- - 1.0 \cdot \mathrm{MON}_r^- \\
d\mathrm{MON}_l^- &= -2.5 \cdot \mathrm{MON}_l^- + 1.0 \cdot \mathrm{I}_l^+ + 1.0 \cdot \mathrm{iMI}_l^+ - 5.5 \cdot \mathrm{iMI}_l^- - 1.0 \cdot \mathrm{MON}_l^- - 1.0 \cdot \mathrm{CMI}_r^- \\
d\mathrm{SMI}_l &= -2.5 \cdot \mathrm{SMI}_l + 1.0 \cdot \mathrm{I}_l^+ + 1.0 \cdot \mathrm{iMI}_l^+ - 1.0 \cdot \mathrm{MON}_l^- - 1.0 \cdot \mathrm{CMI}_r^- \\
d\mathrm{MY}_l &= -2.5 \cdot \mathrm{MY}_l + 1.0 \cdot \mathrm{SMI}_l + 1.0 \cdot \mathrm{SMI}_r
\end{aligned}
$$

Right hemisphere:

$$
\begin{aligned}
d\mathrm{I}_r^+ &= -2.5 \cdot \mathrm{I}_r^+ + \mathrm{Stim}_r(t) \\
d\mathrm{iMI}_r^+ &= -2.5 \cdot \mathrm{iMI}_r^+ + 1.0 \cdot \mathrm{I}_r^+ + 1.0 \cdot \mathrm{iMI}_r^+ - 1.0 \cdot \mathrm{MON}_r^- - 1.0 \cdot \mathrm{CMI}_l^- \\
d\mathrm{iMI}_r^- &= -2.5 \cdot \mathrm{iMI}_r^- + 1.0 \cdot \mathrm{iMI}_r^+ \\
d\mathrm{CMI}_r^- &= -2.5 \cdot \mathrm{CMI}_r^- + 1.0 \cdot \mathrm{iMI}_r^+ - 1.0 \cdot \mathrm{MON}_r^- - 1.0 \cdot \mathrm{CMI}_l^- - 1.0 \cdot \mathrm{MON}_l^- \\
d\mathrm{MON}_r^- &= -2.5 \cdot \mathrm{MON}_r^- + 1.0 \cdot \mathrm{I}_r^+ + 1.0 \cdot \mathrm{iMI}_r^+ - 5.5 \cdot \mathrm{iMI}_r^- - 1.0 \cdot \mathrm{MON}_r^- - 1.0 \cdot \mathrm{CMI}_l^- \\
d\mathrm{SMI}_r &= -2.5 \cdot \mathrm{SMI}_r + 1.0 \cdot \mathrm{I}_r^+ + 1.0 \cdot \mathrm{iMI}_r^+ - 1.0 \cdot \mathrm{MON}_r^- - 1.0 \cdot \mathrm{CMI}_l^- \\
d\mathrm{MY}_r &= -2.5 \cdot \mathrm{MY}_r + 1.0 \cdot \mathrm{SMI}_r + 1.0 \cdot \mathrm{SMI}_l
\end{aligned}
$$

with $rate(t) = rate(t-1) + drate \cdot dt$. I_l^+ and I_r^+ represent signals in the pretectum, thalamus, and optic tectum. We prevented negative activity rates by setting values to zero whenever they became negative in the updating loop. To generate the activity rate plots in **Fig. 5d**, we computed rates relative to baseline (averaging 10 s before motion onset) as $\Delta r / r_0$ matching our imaging analysis of fluorescent data ($\Delta F / F_0$) for better comparisons between model and experiment. To compute rise times, we measured the delay to 90% of the maximal rate per cell type. To compute decay times, we picked the value at the end of the stimulation period and computed the delay until the signal reached 10% of this value. In the MON silencing experiment (**Extended Data Fig. 9b**), we clamped $\mathrm{MON}_l^-(t) = 0$ and $\mathrm{MON}_r^-(t) = 0$.

Following our previously proposed scheme (Bahl and Engert, 2020), we generated an alternative connectivity diagram of cells in the anterior hindbrain (**Extended Data Fig. 9f,g**). Structural and neurotransmitter properties had previously been constrained only by functional imaging, without using precise anatomical or molecular analyses. We used the same modeling framework as for our new model, but with different weights across cell types:

Left hemisphere:

$$
\begin{aligned}
d\mathrm{I}_l^+ &= -2.5 \cdot \mathrm{I}_l^+ + \mathrm{Stim}_l(t) \\
d\mathrm{iMI}_l^+ &= -2.5 \cdot \mathrm{iMI}_l^+ + 1.0 \cdot \mathrm{I}_l^+ + 1.0 \cdot \mathrm{iMI}_l^+ - 1.0 \cdot \mathrm{CMI}_r^- \\
d\mathrm{CMI}_l^- &= -2.5 \cdot \mathrm{CMI}_l^- + 1.0 \cdot \mathrm{iMI}_l^+ \\
d\mathrm{MON}_l^- &= -2.5 \cdot \mathrm{MON}_l^- + 1.0 \cdot \mathrm{I}_l^+ - 3.0 \cdot \mathrm{CMI}_l^- \\
d\mathrm{SMI}_l &= -2.5 \cdot \mathrm{SMI}_l + 1.0 \cdot \mathrm{iMI}_l^+ - 1.0 \cdot \mathrm{MON}_l^-
\end{aligned}
$$

Right hemisphere:

$$
\begin{aligned}
d\mathrm{I}_r^+ &= -2.5 \cdot \mathrm{I}_r^+ + \mathrm{Stim}_r(t) \\
d\mathrm{iMI}_r^+ &= -2.5 \cdot \mathrm{iMI}_r^+ + 1.0 \cdot \mathrm{I}_r^+ + 1.0 \cdot \mathrm{iMI}_r^+ - 1.0 \cdot \mathrm{CMI}_l^- \\
d\mathrm{CMI}_r^- &= -2.5 \cdot \mathrm{CMI}_r^- + 1.0 \cdot \mathrm{iMI}_r^+ \\
d\mathrm{MON}_r^- &= -2.5 \cdot \mathrm{MON}_r^- + 1.0 \cdot \mathrm{I}_r^+ - 3.0 \cdot \mathrm{CMI}_r^- \\
d\mathrm{SMI}_r &= -2.5 \cdot \mathrm{SMI}_r + 1.0 \cdot \mathrm{iMI}_r^+ - 1.0 \cdot \mathrm{MON}_r^-
\end{aligned}
$$

Rise and decay time analyses were implemented in the same way as described above.

Data availability

All neurons described in this paper are browsable in FishExplorer: https://fishexplorer.zib.de/sandbox/.

Github code: https://github.com/arminbahl/Hb_structure_function

Funding

A.B., F.K., K.S., and K.N.K. were supported through the Emmy Noether Program (BA 5923/1-1), the Zukunftskolleg Konstanz, the German Excellence Strategy (EXC 2117-422037984) as well as via a European Research Council (ERC) Starting Grant (N° 101075541; 'CollectiveDecisions'). J.B.W., F.K., G.F.P.S, M.P., Y. W., K.N.K., F.D.B., F.E., and J.W.L. received funding from the Institutes of Health U19 Program (U19NS104653 and 1R01NS124017-01). F.D.B received funding from the Programme Investissements d'Avenir IHU FOReSIGHT ANR-18-IAHU-01 and European Research Council (ERC) N° 101071583 'TubulinCode'. J.B.W. received funding from the Philippe Foundation Inc. F.E. was also supported by the Simons Foundation (SCGB 542973 and NC-GB-CULM-00003241-02). G.F.P.S received funding from the Swiss National Science Foundation (Fellowships P2EZP3_188017 and P500PB_203130). K.S. was supported through a Boehringer Ingelheim Fonds PhD Fellowship.

Author contributions

Project conceptualization: J.B.W., A.B.; Project lead: J.W.L., F.E., F.D.B., A.B.; EM Protocol development for FCLEM and WBEM datasets.: J.B.W., M.P., R.L.S.; FCLEM sample preparation: J.B.W.; FCLEM sample imaging: J.B.W., R.L.S.; Development of EM image quality assessment tools: Y.W.; Electroporations: S.R.; Area photoactivations: S.R., A.B.; X- ray imaging and analysis: J.B.W.; FCLEM sample sectioning: R.L.S.; EM images stitching and coarse elastic alignment: Y.W.; Two-photon imaging and analysis: J.B.W., A.B., F.K., K.S., K.N.K.; 2P to EM image registration: J.B.W., A.B.; Neuronal tracing in FCLEM dataset: J.B.W., J.H.S.; FCLEM dataset connectome analysis: J.B.W.; Single-cell photoactivations: F.K.; Datasets synchronization: F.K.; Development and testing of LDA-based classifier: F.K., J.B.W., G.F.P.S., S.V.; Cross-modality prediction of functional morphotypes: F.K.; Rendering of neuronal morphologies: J.B.W., G.F.P.S., F.K., K.J.H.; Cross-modality neuronal morphology registration: A.B. Modeling: A.B.; HCR FISH: F.K., H.N.; Atlas management: S.V., D.B.; NBLAST quantification: M.E., F.K., S.V.; WBEM sample preparation: M.P., R.L.S.; WBEM sample imaging: M.P., J.B.W., R.L.S.; Neuronal tracing in WBEM dataset: G.F.P.S., K.J.H., R.T., M.S., A.H., D.H., S.D., R.C.W., L.L.Z.; WBEM dataset connectome analysis: G.F.P.S., R.T., K.J.H., J.B.W., K.S.; H2B-GCaMP7f transgenic line generation: I.H.B.; cyto-GCaMP8s transgenic line generation: H.N.; Funding acquisition: J.W.L., F.E., F.D.B., D.B., A.B. Conceptualization of figures: J.B.W., F.K., G.F.P.S., A.B.; Writing of manuscript: All authors provided input to the writing of the manuscript; Correspondence and requests for materials should be addressed to J.B.W. and A.B.

Acknowledgments

We thank Zetta AI for alignment, cell segmentation, synapse detection & assignment, and hosting CAVE. We are grateful to Thomas Macrina for his assistance with connectome analysis, Paul Teufel for his initial help with segmentation, Zachary Miller for his contributions to manual registration, and Hillary Jean-Gilles for her help with tracing.

Bibliography

Akerman, C.J. and Cline, H.T. (2006) 'Depolarizing GABAergic Conductances Regulate the Balance of Excitation to Inhibition in the Developing Retinotectal Circuit *In Vivo*', *The Journal of Neuroscience*, 26(19), pp. 5117–5130. Available at: https://doi.org/10.1523/JNEUROSCI.0319-06.2006.

Ammer, G. *et al.* (2023) 'Multilevel visual motion opponency in Drosophila', *Nature Neuroscience*, 26, pp. 1894–1905. Available at: https://doi.org/10.1038/s41593-023-01443-z.

Arshadi, C. *et al.* (2021) 'SNT: a unifying toolbox for quantification of neuronal anatomy', *Nature Methods*, 18(4), pp. 374–377. Available at: https://doi.org/10.1038/s41592-021-01105-7.

Avants, B.B., Tustison, N. and Johnson, H. (2015) 'Advanced Normalization Tools (ANTS)'.

Bae, J.A. *et al.* (2018) 'Digital Museum of Retinal Ganglion Cells with Dense Anatomy and Physiology', *Cell*, 173(5), pp. 1293-1306.e19. Available at: https://doi.org/10.1016/j.cell.2018.04.040.

Bahl, A. and Engert, F. (2020) 'Neural circuits for evidence accumulation and decision making in larval zebrafish', *Nature Neuroscience*, 23(1), pp. 94–102. Available at: https://doi.org/10.1038/s41593-019-0534-9.

Bargmann, C.I. and Marder, E. (2013) 'From the connectome to brain function.', *Nature methods*, 10(6), pp. 483–90.

Bianco, I.H. *et al.* (2012) 'The Tangential Nucleus Controls a Gravito-inertial Vestibulo-ocular Reflex', *Current Biology*, 22(14), pp. 1285–1295. Available at: https://doi.org/10.1016/j.cub.2012.05.026.

Bogovic, J.A. *et al.* (2016) 'Robust registration of calcium images by learned contrast synthesis', in *2016 IEEE 13th International Symposium on Biomedical Imaging (ISBI)*. *2016 IEEE 13th International Symposium on Biomedical Imaging (ISBI 2016)*, Prague, Czech Republic: IEEE, pp. 1123–1126. Available at: https://doi.org/10.1109/ISBI.2016.7493463.

Boulanger-Weill, J. *et al.* (2017) 'Functional Interactions between Newborn and Mature Neurons Leading to Integration into Established Neuronal Circuits', *Current Biology*, 27(12), pp. 1707-1720.e5. Available at: https://doi.org/10.1016/j.cub.2017.05.029.

Briggman, K.L., Helmstaedter, M. and Denk, W. (2011) 'Wiring specificity in the direction-selectivity circuit of the retina', *Nature*, 471(7337), pp. 183–188. Available at: https://doi.org/10.1038/nature09818.

Brody, C.D. and Hanks, T.D. (2016) 'Neural underpinnings of the evidence accumulator', *Current Opinion in Neurobiology*, 37, pp. 149–157. Available at: https://doi.org/10.1016/j.conb.2016.01.003.

Chen, X. *et al.* (2018) 'Brain-wide Organization of Neuronal Activity and Convergent Sensorimotor Transformations in Larval Zebrafish', *Neuron*, 100(4), pp. 876-890.e5. Available at: https://doi.org/10.1016/j.neuron.2018.09.042.

Choi, H.M.T. *et al.* (2018) 'Third-generation *in situ* hybridization chain reaction: multiplexed,

1201 quantitative, sensitive, versatile, robust', *Development*, 145(12), p. dev165753. Available at:
1202 https://doi.org/10.1242/dev.165753.

1203 Choi, K., Kim, W.K. and Hyeon, C. (2023) 'Polymer Physics-Based Classification of Neurons',
1204 *Neuroinformatics*, 21(1), pp. 177–193. Available at: https://doi.org/10.1007/s12021-022-09605-3.

1205 Costa, M. *et al.* (2016) 'NBLAST: Rapid, Sensitive Comparison of Neuronal Structure and
1206 Construction of Neuron Family Databases', *Neuron*, 91(2), pp. 293–311. Available at:
1207 https://doi.org/10.1016/j.neuron.2016.06.012.

1208 Dana, H. *et al.* (2019) 'High-performance calcium sensors for imaging activity in neuronal
1209 populations and microcompartments', *Nature Methods*, 16(7), pp. 649–657. Available at:
1210 https://doi.org/10.1038/s41592-019-0435-6.

1211 Dombrovski, M. *et al.* (2023) 'Synaptic gradients transform object location to action', *Nature*,
1212 613(7944), pp. 534–542. Available at: https://doi.org/10.1038/s41586-022-05562-8.

1213 Dorkenwald, S. *et al.* (2023) 'CAVE: Connectome Annotation Versioning Engine'. Available at:
1214 https://doi.org/10.1101/2023.07.26.550598.

1215 Dorkenwald, S. *et al.* (2024) 'Neuronal wiring diagram of an adult brain', *Nature*, 634(8032), pp.
1216 124–138. Available at: https://doi.org/10.1038/s41586-024-07558-y.

1217 Dowell, C.K. *et al.* (2024) 'Kinematically distinct saccades are used in a context-dependent manner
1218 by larval zebrafish', *Current Biology*, 34(19), pp. 4382-4396.e5. Available at:
1219 https://doi.org/10.1016/j.cub.2024.08.008.

1220 Dragomir, E.I., Štih, V. and Portugues, R. (2020) 'Evidence accumulation during a sensorimotor
1221 decision task revealed by whole-brain imaging', *Nature Neuroscience*, 23(1), pp. 85–93. Available
1222 at: https://doi.org/10.1038/s41593-019-0535-8.

1223 Feng, L., Zhao, T. and Kim, J. (2015) 'neuTube 1.0: A New Design for Efficient Neuron
1224 Reconstruction Software Based on the SWC Format', *eneuro*, 2(1), p. ENEURO.0049-14.2014.
1225 Available at: https://doi.org/10.1523/ENEURO.0049-14.2014.

1226 Filippi, A., Mueller, T. and Driever, W. (2014) 'vglut2 and gad expression reveal distinct patterns of
1227 dual GABAergic versus glutamatergic cotransmitter phenotypes of dopaminergic and noradrenergic
1228 neurons in the zebrafish brain', *Journal of Comparative Neurology*, 522(9), pp. 2019–2037.
1229 Available at: https://doi.org/10.1002/cne.23524.

1230 Förster, D. *et al.* (2018) 'Optogenetic precision toolkit to reveal form, function and connectivity of
1231 single neurons', *Methods*, 150, pp. 42–48. Available at: https://doi.org/10.1016/j.ymeth.2018.08.012.

1232 Freeman, J. *et al.* (2014) 'Mapping brain activity at scale with cluster computing', *Nature Methods*,
1233 11(9), pp. 941–950. Available at: https://doi.org/10.1038/nmeth.3041.

1234 Friedrich, R.W. and Wanner, A.A. (2021) 'Dense Circuit Reconstruction to Understand Neuronal
1235 Computation: Focus on Zebrafish', *Annual Review of Neuroscience*, 44, pp. 275–293. Available at:
1236 https://doi.org/10.1146/annurev-neuro-110220-013050.

1237 Fujita, M. *et al.* (2011) 'Assembly and patterning of the vascular network of the vertebrate hindbrain',
1238 *Development*, 138(9), pp. 1705–1715. Available at: https://doi.org/10.1242/dev.058776.

1239 Groschner, L.N. *et al.* (2018) 'Dendritic Integration of Sensory Evidence in Perceptual Decision-
1240 Making', *Cell*, 173(4), pp. 894-905.e13. Available at: https://doi.org/10.1016/j.cell.2018.03.075.

1241 Hanks, T.D. *et al.* (2015) 'Distinct relationships of parietal and prefrontal cortices to evidence
1242 accumulation', *Nature*, 520(7546), pp. 220–223. Available at: https://doi.org/10.1038/nature14066.

1243 Hanks, T.D. and Summerfield, C. (2017) 'Perceptual Decision Making in Rodents, Monkeys, and
1244 Humans', *Neuron*, 93(1), pp. 15–31. Available at: https://doi.org/10.1016/j.neuron.2016.12.003.

1245 Hayworth, K.J. *et al.* (2014) 'Imaging ATUM ultrathin section libraries with WaferMapper: a multi-
1246 scale approach to EM reconstruction of neural circuits', *Frontiers in Neural Circuits*, 8. Available at:
1247 https://doi.org/10.3389/fncir.2014.00068.

1248 Henriques, P.M. *et al.* (2019) 'Nucleus Isthmi Is Required to Sustain Target Pursuit during Visually
1249 Guided Prey-Catching', *Current Biology*, 29(11), pp. 1771-1786.e5. Available at:
1250 https://doi.org/10.1016/j.cub.2019.04.064.

1251 Higashijima, S.-I., Mandel, G. and Fetcho, J.R. (2004) 'Distribution of prospective glutamatergic,
1252 glycinergic, and GABAergic neurons in embryonic and larval zebrafish', *The Journal of Comparative*
1253 *Neurology*, 480(1), pp. 1–18. Available at: https://doi.org/10.1002/cne.20278.

1254 Hildebrand, D.G.C. *et al.* (2017) 'Whole-brain serial-section electron microscopy in larval zebrafish',
1255 *Nature* [Preprint]. Available at: https://doi.org/10.1038/nature22356.

1256 Holler, S. *et al.* (2021) 'Structure and function of a neocortical synapse', *Nature*, 591(7848), pp.
1257 111–116. Available at: https://doi.org/10.1038/s41586-020-03134-2.

1258 Hua, Y., Laserstein, P. and Helmstaedter, M. (2015) 'Large-volume en-bloc staining for electron
1259 microscopy-based connectomics', *Nature Communications*, 6(1), p. 7923. Available at:
1260 https://doi.org/10.1038/ncomms8923.

1261 Joy, D.C. (2002) 'SMART BlackwellScience,Ltd – a program to measure SEM resolution and
1262 imaging performance', *Journal of Microscopy* [Preprint].

1263 Kappel, J.M. *et al.* (2022) 'Visual recognition of social signals by a tectothalamic neural circuit',
1264 *Nature*, 608(7921), pp. 146–152. Available at: https://doi.org/10.1038/s41586-022-04925-5.

1265 Katz, L.N. *et al.* (2016) 'Dissociated functional significance of decision-related activity in the primate
1266 dorsal stream', *Nature*, 535(7611), pp. 285–288. Available at: https://doi.org/10.1038/nature18617.

1267 Kawashima, T. *et al.* (2016) 'The Serotonergic System Tracks the Outcomes of Actions to Mediate
1268 Short-Term Motor Learning', *Cell*, 167(4), pp. 933-946.e20. Available at:
1269 https://doi.org/10.1016/j.cell.2016.09.055.

1270 Kawashima, T. *et al.* (2024) 'Voltage imaging reveals circuit computations in the raphe underlying
1271 serotonin-mediated motor vigor learning'. Neuroscience. Available at:
1272 https://doi.org/10.1101/2024.09.15.613083.

1273 Khona, M. and Fiete, I.R. (2022) 'Attractor and integrator networks in the brain', *Nature Reviews*
1274 *Neuroscience*, 23(12), pp. 744–766. Available at: https://doi.org/10.1038/s41583-022-00642-0.

1275 Kramer, A. *et al.* (2019) 'Neuronal architecture of a visual center that processes optic flow', *Neuron*,
1276 103(1), pp. 118-132.e7. Available at: https://doi.org/10.1016/j.neuron.2019.04.018.

1277 Kubo, F. *et al.* (2014a) 'Functional Architecture of an Optic Flow-Responsive Area that Drives
1278 Horizontal Eye Movements in Zebrafish', *Neuron*, 81(6), pp. 1344–1359. Available at:
1279 https://doi.org/10.1016/j.neuron.2014.02.043.

1280 Kubo, F. *et al.* (2014b) 'Functional Architecture of an Optic Flow-Responsive Area that Drives
1281 Horizontal Eye Movements in Zebrafish', *Neuron*, 81(6), pp. 1344–1359. Available at:
1282 https://doi.org/10.1016/j.neuron.2014.02.043.

1283 Kunst, M. *et al.* (2019) 'A Cellular-Resolution Atlas of the Larval Zebrafish Brain', *Neuron*, 103(1),
1284 pp. 21-38.e5. Available at: https://doi.org/10.1016/j.neuron.2019.04.034.

1285 Lanciego, J.L., Luquin, N. and Obeso, J.A. (2012) 'Functional Neuroanatomy of the Basal Ganglia',
1286 *Cold Spring Harbor Perspectives in Medicine*, 2(12), pp. a009621–a009621. Available at:
1287 https://doi.org/10.1101/cshperspect.a009621.

1288 Lappalainen, J.K. *et al.* (2024) 'Connectome-constrained networks predict neural activity across the
1289 fly visual system', *Nature*, pp. 1–9. Available at: https://doi.org/10.1038/s41586-024-07939-3.

1290 Lee, W.-C.A. *et al.* (2016) 'Anatomy and function of an excitatory network in the visual cortex',
1291 *Nature*, 532(7599), pp. 370–374. Available at: https://doi.org/10.1038/nature17192.

1292 Li, Y. *et al.* (2017) 'Metrics for comparing neuronal tree shapes based on persistent homology',
1293 *PLOS ONE*, 12(8), p. e0182184. Available at: https://doi.org/10.1371/journal.pone.0182184.

1294 Lister, J.A. *et al.* (1999) 'nacre encodes a zebrafish microphthalmia-related protein that regulates
1295 neural-crest-derived pigment cell fate', *Development*, 126(17), pp. 3757–3767. Available at:
1296 https://doi.org/10.1242/dev.126.17.3757.

1297 Macrina, T. *et al.* (2021) 'Petascale neural circuit reconstruction: automated methods'. Available at:
1298 https://doi.org/10.1101/2021.08.04.455162.

1299 Naumann, E.A. *et al.* (2016) 'From Whole-Brain Data to Functional Circuit Models: The Zebrafish
1300 Optomotor Response', *Cell*, 167(4), pp. 947-960.e20. Available at:
1301 https://doi.org/10.1016/j.cell.2016.10.019.

1302 Newsome, W.T., Britten, K.H. and Movshon, J.A. (1989) 'Neuronal correlates of a perceptual
1303 decision', *Nature*, 341(6237), pp. 52–54. Available at: https://doi.org/10.1038/341052a0.

1304 Orger, M.B. *et al.* (2008) 'Control of visually guided behavior by distinct populations of spinal
1305 projection neurons', *Nature Neuroscience*, 11(3), pp. 327–333. Available at:
1306 https://doi.org/10.1038/nn2048.

1307 Pallotto, M. *et al.* (2015) 'Extracellular space preservation aids the connectomic analysis of neural
1308 circuits', *eLife*, 4, p. e08206. Available at: https://doi.org/10.7554/eLife.08206.

1309 Patterson, G.H. and Lippincott-Schwartz, J. (2002) 'A Photoactivatable GFP for Selective
1310 Photolabeling of Proteins and Cells', *Science*, 297(5588), pp. 1873–1877. Available at:
1311 https://doi.org/10.1126/science.1074952.

1312 Petrucco, L. *et al.* (2023) 'Neural dynamics and architecture of the heading direction circuit in
1313 zebrafish', *Nature Neuroscience*, pp. 1–9. Available at: https://doi.org/10.1038/s41593-023-01308-5.

1314 Pnevmatikakis, E.A. and Giovannucci, A. (2017) 'NoRMCorre: An online algorithm for piecewise
1315 rigid motion correction of calcium imaging data', *Journal of Neuroscience Methods*, 291, pp. 83–94.
1316 Available at: https://doi.org/10.1016/j.jneumeth.2017.07.031.

1317 Popovych, S. *et al.* (2024) 'Petascale pipeline for precise alignment of images from serial section
1318 electron microscopy', *Nature Communications*, 15(1), p. 289. Available at:
1319 https://doi.org/10.1038/s41467-023-44354-0.

1320 Randlett, O., Wee, C.L., Naumann, E.A., *et al.* (2015) 'Whole-brain activity mapping onto a zebrafish
1321 brain atlas', *Nature Methods*, 12(11), pp. 1039–1046. Available at:
1322 https://doi.org/10.1038/nmeth.3581.

1323 Randlett, O., Wee, C.L., Naumann, E. a, *et al.* (2015) 'Whole-brain activity mapping onto a zebrafish
1324 brain atlas', *Nature Methods*, 12(September), pp. 1–12. Available at:
1325 https://doi.org/10.1038/nmeth.3581.

1326 Sato, M. *et al.* (2000) 'TEASAR: tree-structure extraction algorithm for accurate and robust

skeletons', in *Proceedings the Eighth Pacific Conference on Computer Graphics and Applications*. *the Eighth Pacific Conference on Computer Graphics and Applications*, Hong Kong, China: IEEE Comput. Soc, pp. 281–449. Available at: https://doi.org/10.1109/PCCGA.2000.883951.

Satou, C. *et al.* (2013) 'Transgenic tools to characterize neuronal properties of discrete populations of zebrafish neurons', *Development*, 140(18), pp. 3927–3931. Available at: https://doi.org/10.1242/dev.099531.

Schindelin, J. *et al.* (2012) 'Fiji: an open-source platform for biological-image analysis', *Nature Methods*, 9(7), pp. 676–682. Available at: https://doi.org/10.1038/nmeth.2019.

Schlegel, P. *et al.* (2024) 'Whole-brain annotation and multi-connectome cell typing of Drosophila', *Nature*, 634(8032), pp. 139–152. Available at: https://doi.org/10.1038/s41586-024-07686-5.

Schlegel, P. *et al.* (2025) 'navis-org/navis: Version 1.10.0'. Zenodo. Available at: https://doi.org/10.5281/zenodo.14827782.

Seung, H.S. (1996) 'How the brain keeps the eyes still', *Proceedings of the National Academy of Sciences*, 93(23), pp. 13339–13344. Available at: https://doi.org/10.1073/pnas.93.23.13339.

Shainer, I. *et al.* (2023) 'A single-cell resolution gene expression atlas of the larval zebrafish brain', *Science Advances*, 9(eade9909). Available at: https://doi.org/10.1126/sciadv.ade9909.

Shapson-Coe, A. *et al.* (2024) 'A petavoxel fragment of human cerebral cortex reconstructed at nanoscale resolution', *Science*, 384(6696), p. eadk4858. Available at: https://doi.org/10.1126/science.adk4858.

Shiu, P.K. *et al.* (2024) 'A Drosophila computational brain model reveals sensorimotor processing', *Nature*, 634(8032), pp. 210–219. Available at: https://doi.org/10.1038/s41586-024-07763-9.

Silversmith, W. *et al.* (2022) 'Igneous: Distributed dense 3D segmentation meshing, neuron skeletonization, and hierarchical downsampling', *Frontiers in Neural Circuits*, 16, p. 977700. Available at: https://doi.org/10.3389/fncir.2022.977700.

Stringer, C. and Pachitariu, M. (2025) 'Cellpose3: one-click image restoration for improved cellular segmentation', *Nature Methods*, 22(3), pp. 592–599. Available at: https://doi.org/10.1038/s41592-025-02595-5.

Svara, F. *et al.* (2022) 'Automated synapse-level reconstruction of neural circuits in the larval zebrafish brain', *Nature Methods*, 19(11), pp. 1357–1366. Available at: https://doi.org/10.1038/s41592-022-01621-0.

Tapia, J.C. *et al.* (2012) 'High-contrast en bloc staining of neuronal tissue for field emission scanning electron microscopy', *Nature Protocols*, 7(2), pp. 193–206. Available at: https://doi.org/10.1038/nprot.2011.439.

The MICrONS Consortium *et al.* (2025) 'Functional connectomics spanning multiple areas of mouse visual cortex', *Nature*, 640(8058), pp. 435–447. Available at: https://doi.org/10.1038/s41586-025-08790-w.

Turner, N.L. *et al.* (2022) 'Reconstruction of neocortex: Organelles, compartments, cells, circuits, and activity', *Cell*, 185(6), pp. 1082-1100.e24. Available at: https://doi.org/10.1016/j.cell.2022.01.023.

Turner-Evans, D.B. *et al.* (2020) 'The Neuroanatomical Ultrastructure and Function of a Biological Ring Attractor', *Neuron*, 108(1), pp. 145-163.e10. Available at: https://doi.org/10.1016/j.neuron.2020.08.006.

Umargono, E., Suseno, J.E. and S. K., V.G. (2019) ‘K-Means Clustering Optimization using the Elbow Method and Early Centroid Determination Based-on Mean and Median’:, in *Proceedings of the International Conferences on Information System and Technology*. *International Conferences on Information System and Technology*, Yogyakarta, Indonesia: SCITEPRESS - Science and Technology Publications, pp. 234–240. Available at: https://doi.org/10.5220/0009908402340240.

Vishwanathan, A. *et al.* (2017) ‘Electron Microscopic Reconstruction of Functionally Identified Cells in a Neural Integrator’, *Current Biology*, 27(14), pp. 2137-2147.e3. Available at: https://doi.org/10.1016/j.cub.2017.06.028.

Vishwanathan, A. *et al.* (2024) ‘Predicting modular functions and neural coding of behavior from a synaptic wiring diagram’, *Nature Neuroscience*, pp. 1–12. Available at: https://doi.org/10.1038/s41593-024-01784-3.

Wang, K. *et al.* (2019) ‘Selective processing of all rotational and translational optic flow directions in the zebrafish pretectum and tectum’, *BMC Biology*, 17(1), p. 29. Available at: https://doi.org/10.1186/s12915-019-0648-2.

Wanner, A.A. and Friedrich, R.W. (2020) ‘Whitening of odor representations by the wiring diagram of the olfactory bulb’, *Nature Neuroscience*, 23(3), pp. 433–442. Available at: https://doi.org/10.1038/s41593-019-0576-z.

Weigert, M. *et al.* (2018) ‘Content-aware image restoration: pushing the limits of fluorescence microscopy’, *Nature Methods*, 15(12), pp. 1090–1097. Available at: https://doi.org/10.1038/s41592-018-0216-7.

Weigert, M. *et al.* (2020) ‘Star-convex Polyhedra for 3D Object Detection and Segmentation in Microscopy’, in *2020 IEEE Winter Conference on Applications of Computer Vision (WACV)*. *2020 IEEE Winter Conference on Applications of Computer Vision (WACV)*, Snowmass Village, CO, USA: IEEE, pp. 3655–3662. Available at: https://doi.org/10.1109/WACV45572.2020.9093435.

Weigert, M. and Schmidt, U. (2022) ‘Nuclei Instance Segmentation and Classification in Histopathology Images with Stardist’, in *2022 IEEE International Symposium on Biomedical Imaging Challenges (ISBIC)*. *2022 IEEE International Symposium on Biomedical Imaging Challenges (ISBIC)*, Kolkata, India: IEEE, pp. 1–4. Available at: https://doi.org/10.1109/ISBIC56247.2022.9854534.

Witvliet, D. *et al.* (2021) ‘Connectomes across development reveal principles of brain maturation’, *Nature*, 596(7871), pp. 257–261. Available at: https://doi.org/10.1038/s41586-021-03778-8.

Wolf, S. *et al.* (2017) ‘Sensorimotor computation underlying phototaxis in zebrafish’, *Nature Communications*, 8(1), p. 651. Available at: https://doi.org/10.1038/s41467-017-00310-3.

Yang, R. *et al.* (2023) ‘Cyclic structure with cellular precision in a vertebrate sensorimotor neural circuit’, *Current Biology*, 33(11), pp. 2340-2349.e3. Available at: https://doi.org/10.1016/j.cub.2023.05.010.

Zhang, Y. *et al.* (2023) ‘Fast and sensitive GCaMP calcium indicators for imaging neural populations’, *Nature*, 615(7954), pp. 884–891. Available at: https://doi.org/10.1038/s41586-023-05828-9.

Zou, M., Friedrich, R.W. and Bianco, I.H. (2016) ‘Targeted Electroporation in Embryonic, Larval, and Adult Zebrafish’, in K. Kawakami, E.E. Patton, and M. Orger (eds) *Zebrafish: Methods and Protocols*. New York, NY: Springer New York, pp. 259–269. Available at: https://doi.org/10.1007/978-1-4939-3771-4_17.

Extended Data

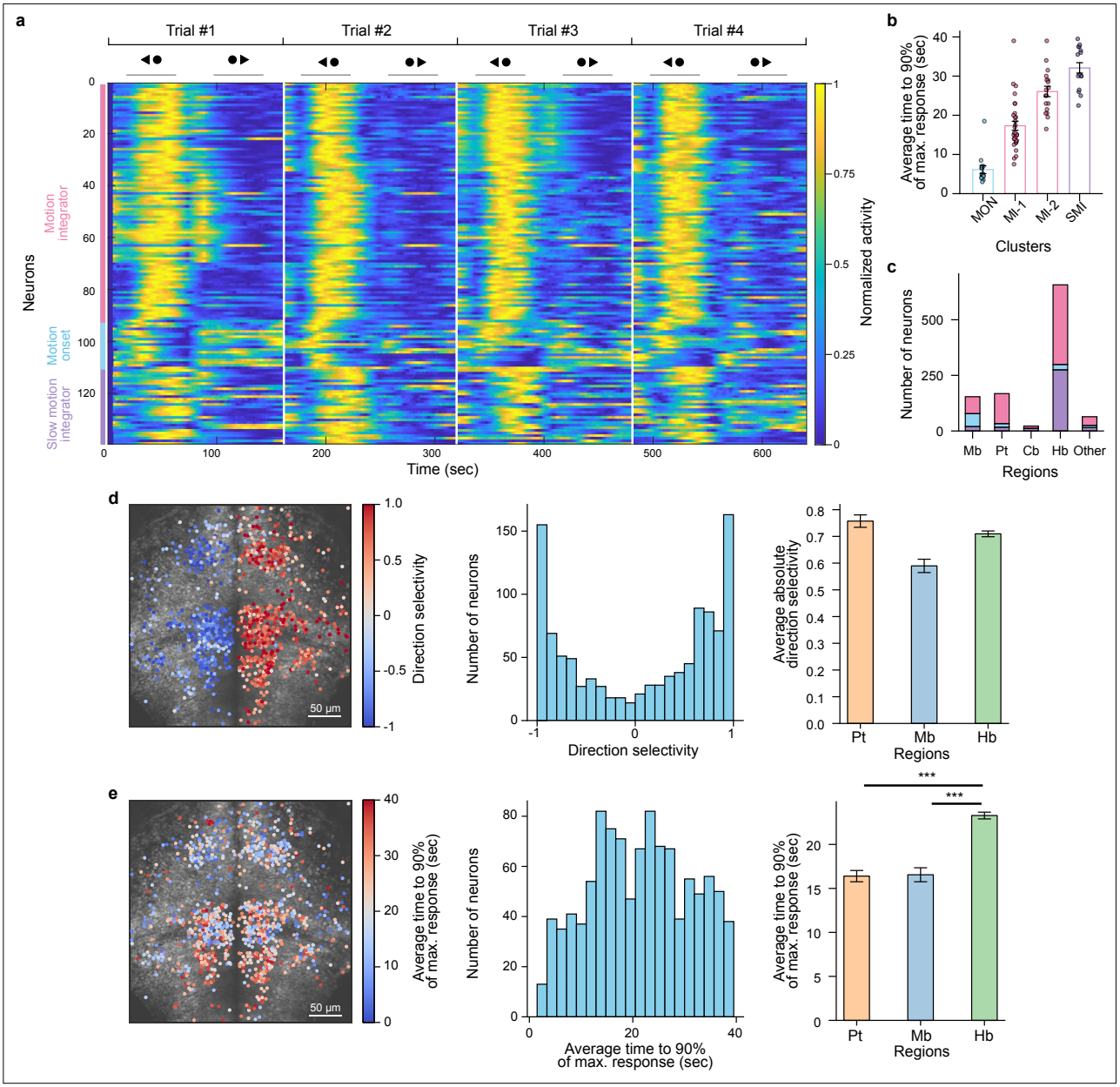

Extended Data Fig. 1 | Detailed analysis of neuronal functional recordings. (a) Raster plot of representative examples of direction-selective neurons belonging to the three functional classes. Four example trials, both for left- and rightward-moving dots. The upper arrows represent the direction of motion and the gray bars represent the stimulation epochs. Neurons are organized according to their functional responses (see left colored bars). Individual trials are separated by horizontal white bars. **(b)** Rise time to reach 90% of the maximal response for each k-means cluster. Each dot represents a single neuron. MON, motion onset neurons; MI-1, fast motion integrators; MI-2, intermediate motion integrators; SMI, slow motion integrators. **(c)** Distribution of neurons across brain regions and cluster types. (**d**) Left: spatial distribution of direction selectivity values for the three functional classes. Middle: histogram of direction selectivity values for the same population. Right: average values for neurons grouped by brain region. *** indicates $p < 0.001$ (two-sided t-test), (**e**) Same as in (**d**) but for representing the time to reach 90% of the maximal response. Mb, midbrain; Pt, pretectum; Cb, cerebellum; Hb, hindbrain; Oth, other regions.

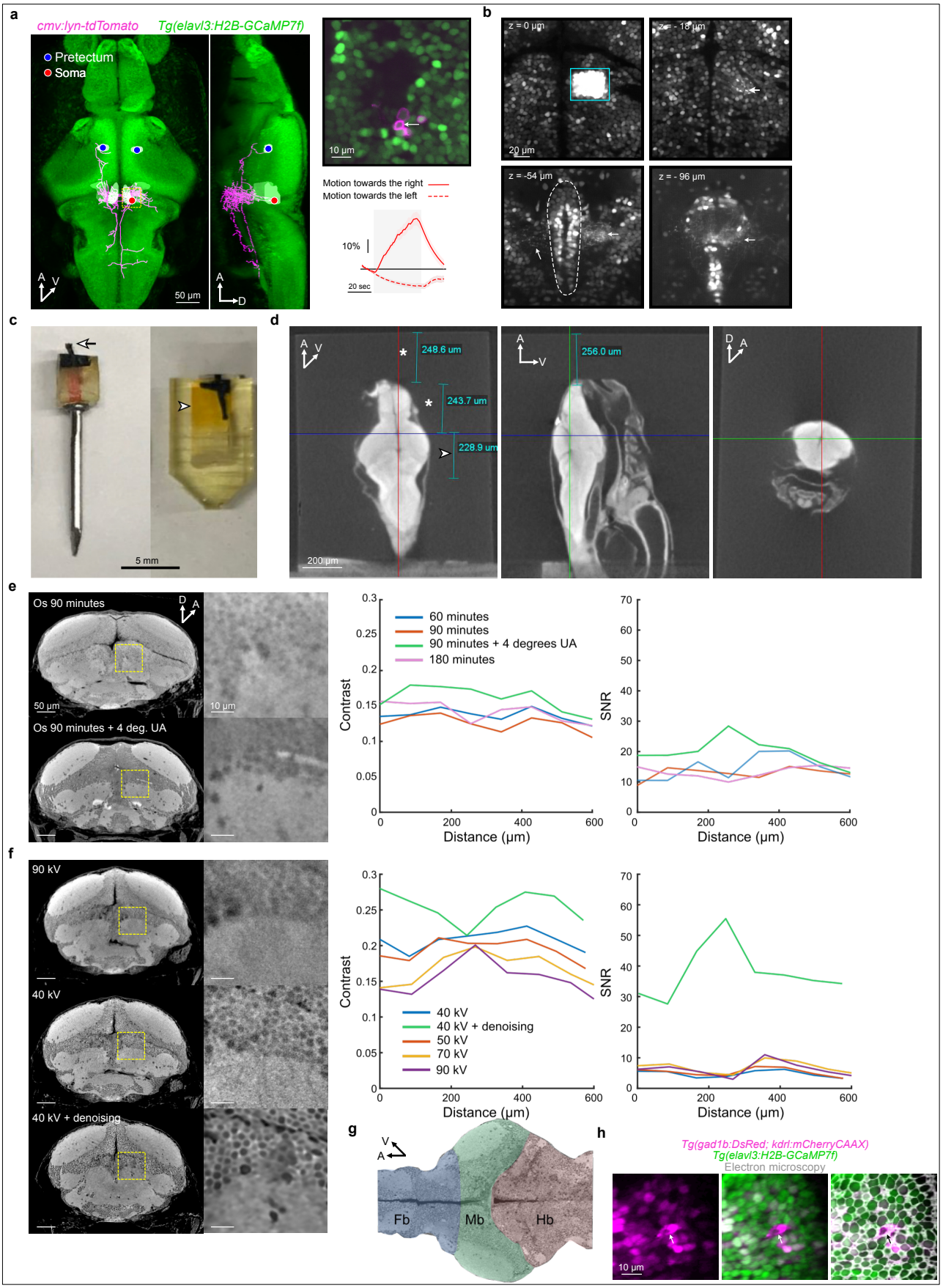

Extended Data Fig. 2 | Sample preparation and region of interest identification. a, hindbrain sparse electroporations. Left panels: reconstructed neurons registered to a reference brain indicating soma and Pt locations. Note the projection pattern of the cells towards the Pt and ipsilateral and contralateral anterior hindbrain. The dashed yellow square is magnified in the top-right snippet. Right panels: two-photon single-plane image showing the somas of the electroporated neurons together with response dynamics to rightward and leftward moving dots for one neuron (indicated by the white arrow). The

activity responses are reminiscent of an evidence integrator. Activity traces show the average responses for 4 trials (SEM indicated by the red-shaded area). The stimulation epoch is denoted by the shaded gray area. **b**, Photoactivation of a group of neurons in the anterior hindbrain in *Tg(elavl3:H2B-GCaMP6s, gad1b:loxP-DsRed-loxP-GFP, alpha-tub:c3pa-GFP)* (cyan square). Cells project ventrally, ipsilaterally, and contralaterally close to the raphe (dashed outline at z=–54 µm from the photoactivation plane). Neuronal projections are indicated by the white arrows. **c,** Left: A resin-embedded larva with the cast around the head trimmed (white arrow) for enhanced X-ray penetration. Right: Another larva re-embedded in resin after X-ray tomography before ultramicrotome sectioning. The limit between the two resin casts is denoted by the arrowhead. **d,** Orthogonal X-ray tomography views of the main larva used in this study. The first panel shows the edges of the region of interest determined before the section collection. By performing direct measurements using the X-ray microscope software we precisely targeted the section collection by trimming away the unnecessary resin and tissue (white asterisks), keeping only the region of interest (white arrowhead) containing the anterior hindbrain and most of the identified neuronal projections (**a,b**). **e,** The First step of contrast and signal-to-noise ratio (SNR) improvement was achieved by varying the Osmium (Os) incubation duration and incubating the Uranyl Acetate (UA) at 4°C instead of room temperature. Left panels: Representative X-ray tomography cross sections along the main axis of the larva and high-resolution snippets (corresponding to dashed yellow squares). Right panels: Contrast and SNR computed along the main axis of the fish, see **Extended Data Fig. 2g**. Each line represents the average of two fish per condition. **f,** Similar to (**i**) showing the improvement by changing the X-ray imaging power. Notice the dose-dependent improvement as the power is lowered from 90 to 40 kV. **g,** Reference fish imaged with X-ray (dorsal section plane) indicating where the contrast and SNR measurements were performed. Distances correspond to the upper plots. Fb, forebrain; Mb, midbrain; Hb, hindbrain. **h,** Images showing the alignment between the 2P and EM datasets confirming the precise correspondence of a blood vessel cross-section (indicated by a white arrow) across imaging modalities. Abbreviations: A, anterior; D, dorsal; V, ventral.

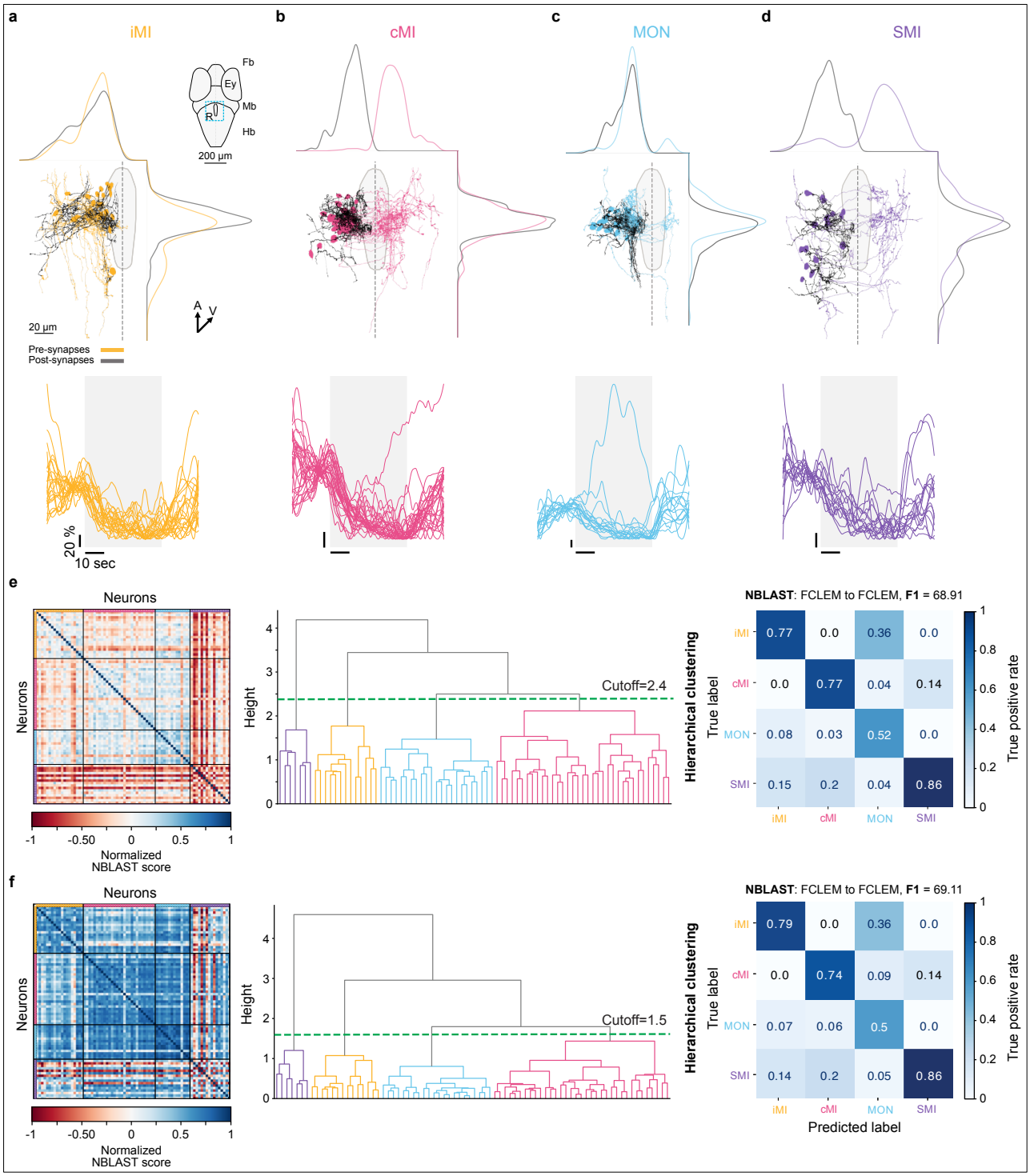

Extended Data Fig. 3 | Structure-function relationship and morphological diversity within and in-between clusters. **a,** Structure-function relationship of functionally imaged and reconstructed iMI neurons as in **Fig. 1f–i** but in dorsal view. Somas and axons are colored in orange and dendrites in black. The dashed line represents the midline. Surrounding plots are the distribution of presynaptic (orange) and postsynaptic (black) synapses along the x (top) and y (right) axes. Right: schematic showing coarse brain organization (dorsal-to-ventral view) and location of the reconstructed neurons below (blue dashed square) and outlines of the raphe (also shown below). Right: traces representing the normalized $\Delta F/F_0$ neuronal activity over time for motion in the opposite, null direction. **b–d**, shows an identical representation for other neuron types. All neurons are registered to a reference brain (Randlett, Wee, E. a Naumann, *et al.*, 2015). Abbreviations: Mb, midbrain; Hb, hindbrain; R, raphe; Ey, eye; A, anterior; V, ventral. **e–f**, Left matrices: Normalized NBLAST matrix organized by functional types using morphological similarity distances computed using *Drosophila* neurons (**e**) and the functionally identified zebrafish neurons in this study (**f**). Middle: dendrogram showing the cutoff required to separate 4 clusters and right, confusion matrices of true positive rate using FCLEM cells as the ground truth and predicting FCLEM cells. F1-score for the entire matrix is indicated in the title.

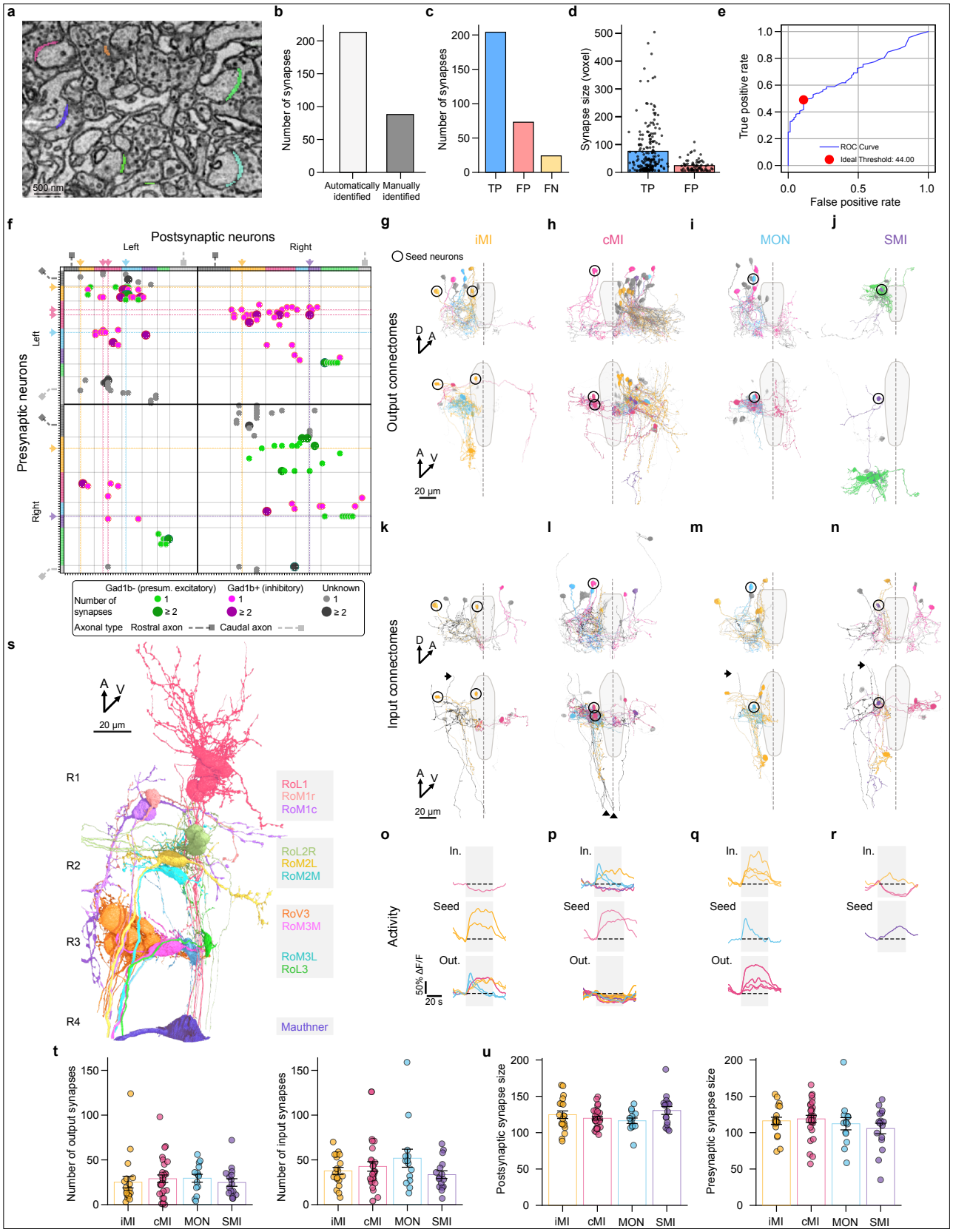

Extended Data Fig. 4 | Details of automated synapse predictions and functional dynamics of reconstructed connectomes examples. a, Raw EM image with automatically detected synaptic clefts in color. **b**, Histogram showing the number of automatically identified and manually identified synapses by visually inspecting two dendrites and one axon. **c**, Classification of automatically predicted synapses as true positives, false positives (not synapses), and false negatives (missing synapses). **d**, Comparison of synapse sizes between true positives and false positives. **e**, Receiver Operating Characteristic (ROC) curve analysis establishing a size threshold at 44 voxels to exclude 90% of false positive synapses. **f**, Connectivity matrix with neurons and connected axons sorted according to their functional types and hemispheres (thick

black bars separate the left and right hemispheres). Rostral axons, truncated at the rostral end of the imaging volume, terminate within the volume, while caudal axons are truncated at the caudal end of the volume and also terminate within it. Axons that traverse the entire imaging volume are not shown. Colored arrows and lines correspond to the example connectomes shown in **g-n.** Representative output (**g-j**) and input (**k-n**) example connectomes (coronal view, top renderings; dorsal view, bottom renderings) for one or two seed cells related to **Fig. 2c–j.** All neuronal parts (soma, axon, and dendrites) are colored identically. All neurons are registered to a reference brain (Randlett, Wee, E. a Naumann, *et al.*, 2015). The dashed line represents the midline. Black arrows and arrowheads represent example rostral and caudal axons, respectively. **o–r,** Activity traces for the neurons shown in this figure **(g–n)** with visual stimulation epochs indicated by gray shaded areas. Dashes black lines correspond to $\Delta F/F_0$. **s,** Rendering of identified reticulospinal neurons belonging to rhombomeres 1 to 4 (R1–4). **t**, Histograms showing the distributions of synapse numbers and sizes (**u**) for each functionally identified cell type. Error bars represent the standard error of the mean (SEM). Individual dots represent single neurons.

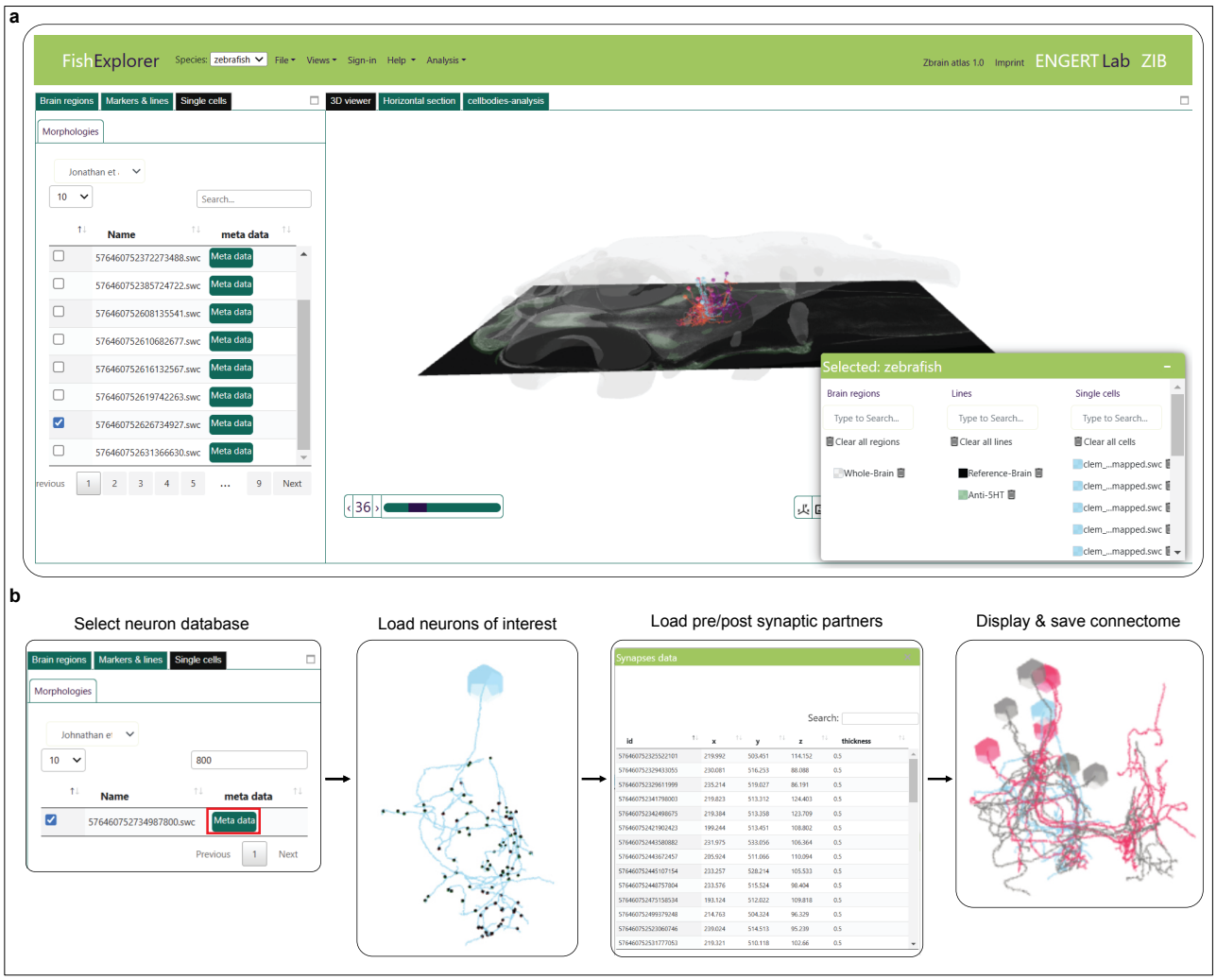

Extended Data Fig. 5 | Online neurons and connectome visualization. (a) Multi-modal and multi-species web-based atlas platform contains annotations of all anatomical brain subdivisions and 294 registered transgenic lines for deeper analyses. **(b)** Flowchart to visualize single neurons and connectomes in FishExplorer. To visualize single cells and connectomes, users should first select the neuron of interest by selecting the appropriate dataset (correlated light and EM, photoactivated neurons, EM whole-brain Atlas) and tracer. To display the connectomes of a cell, users should then click the meta information button in front of the neuron name highlighted by the red rectangle. The window shows meta information, input, and output partners will appear on the screen. Next, the user can load all the output partners by clicking the 'load all output' button. The researchers can also save and share their current analysis 'scene' of connectomes with the community.

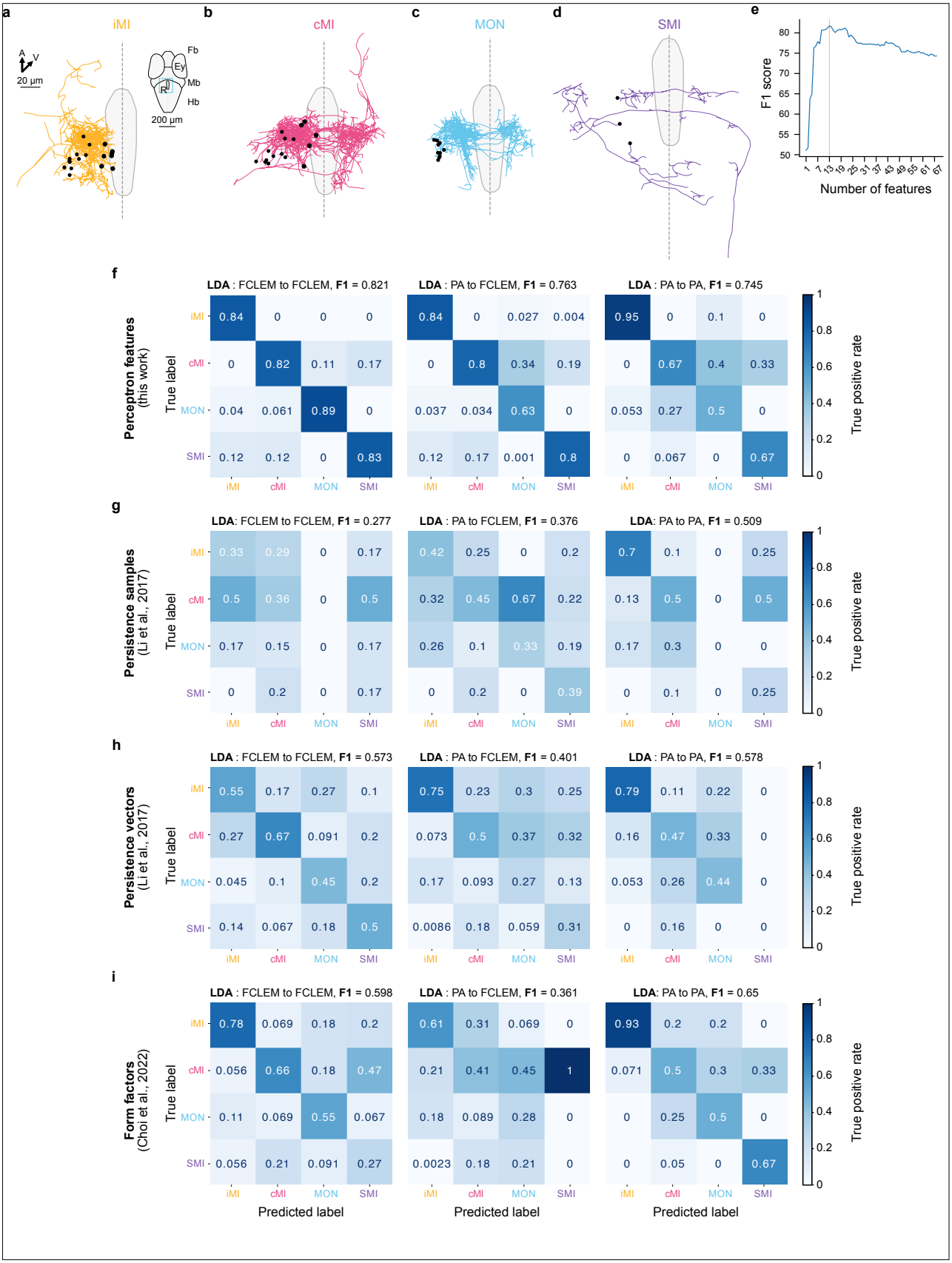

Extended Data Fig. 6 | Photoactivated neurons diversity and LDA benchmarking. a, Structure-function relationship of functionally imaged and photoactivated neurons as in **Fig. 3b–e** but in dorsal view. Right: schematic showing coarse brain organization (dorsal-to-ventral view) and location of the reconstructed neurons below (blue dashed square) and outlines of the raphe (also shown below). **b–d**, shows an identical representation for other neuron types. All neurons are registered to a reference brain (Randlett, Wee, E. a Naumann, *et al.*, 2015). Abbreviations: Mb, midbrain; Hb, hindbrain; R, raphe; Ey, eye; A, anterior; V, ventral. **e**, F1-score as a function of the feature subset size used for **Fig. 3g** and below.

The red line represents the number of features (n=13) yielding the maximum F1-score. **f**, Left, LDA confusion matrix of true positive rate using FCLEM cells as the ground truth and predicting FCLEM cells. F1-score for the entire matrix is indicated in the title. Middle same as left, but using PA as ground truth and predicting FCLEM cells. Right, same as left, but using PA as ground truth and predicting PA cells. LDA, linear discriminant analysis; RF, random forest. **g–i**, Prediction of functional types using other established methods (persistence samples, persistence vectors, and form factors metrics, respectively). The display is identical to that in (**f**).

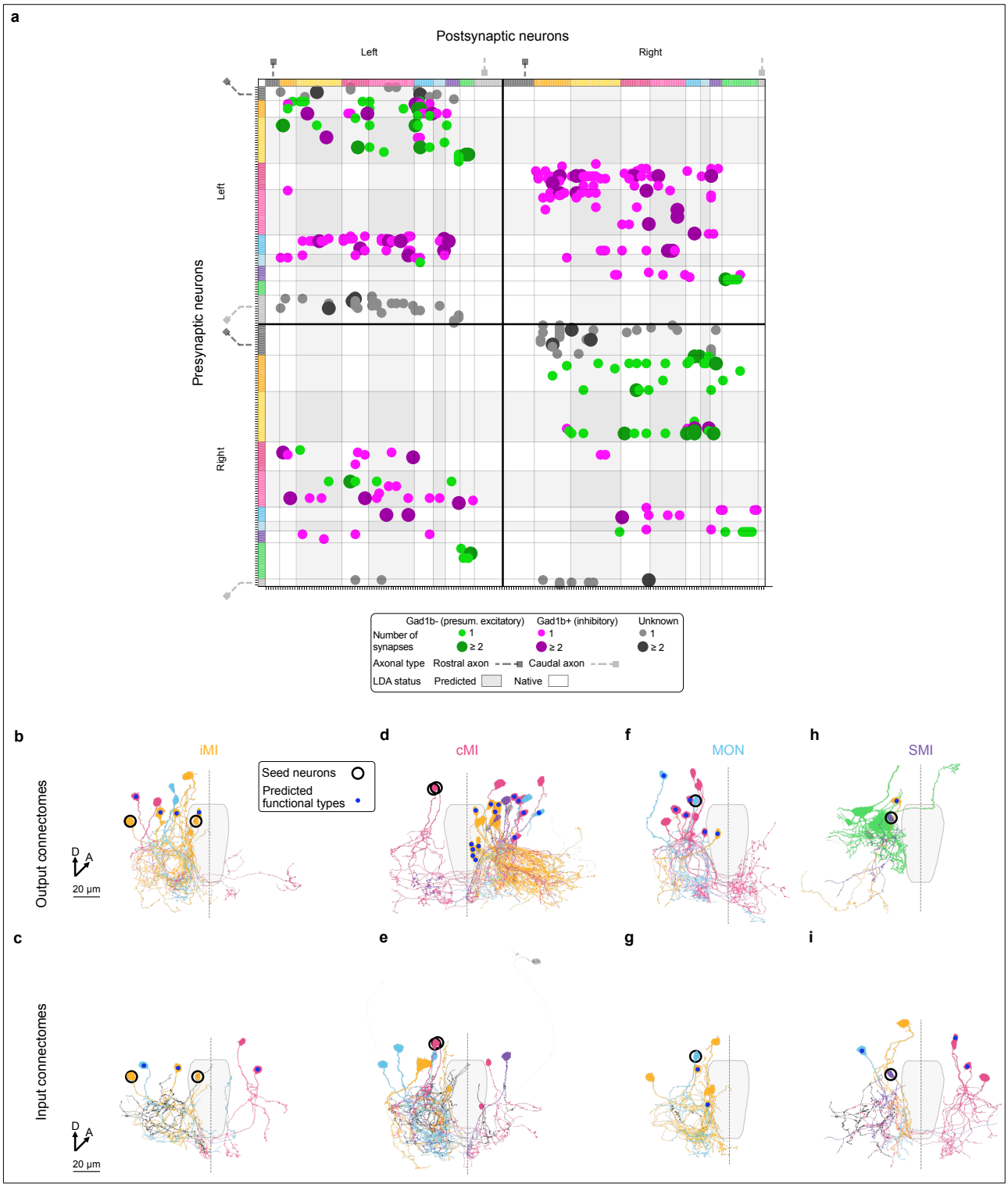

Extended Data Fig. 7 | Enhanced connectome of the zebrafish anterior hindbrain. a, Connectivity matrix with neurons and connected axons sorted according to their functional types and hemispheres (solid black lines). Rostral axons (dark gray), truncated at the rostral end of the imaging volume, terminate within the volume, while caudal axons (light gray) are truncated at the caudal end of the volume and also terminate within it. Axons that traverse the entire imaging volume are not shown. **b–i,** Representative example output and input connectomes (coronal view) for one or two seed cells related to **Fig. 2c–j.** All neuronal parts (soma, axon, and dendrites) are colored identically. All neurons are registered to a reference brain (Randlett, Wee, E. a Naumann, *et al.*, 2015).

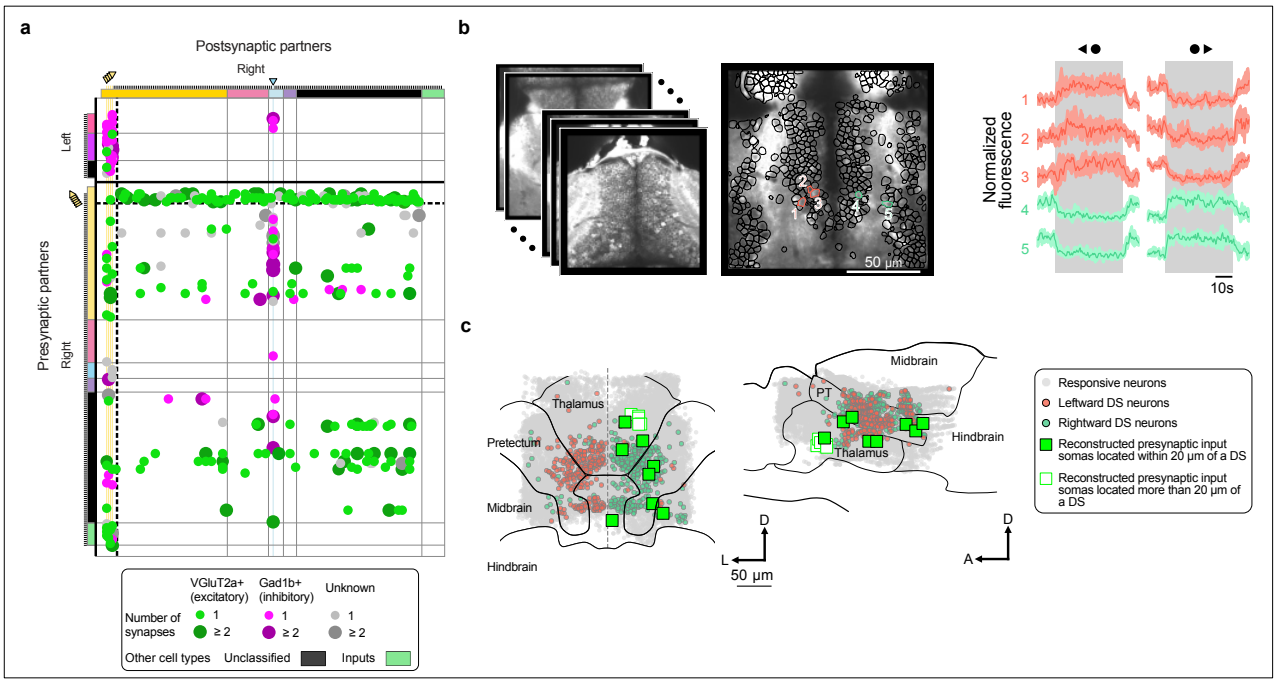

Extended Data Fig. 8 | Full WBEM connectivity matrix and imaging of thalamic, pretectal, and midbrain direction-selective inputs. a, Connectivity matrix for LDA-classified WBEM neurons, organized by morphotype and hemisphere as in **Fig. 4g,** but also with unclassified neurons (black bars). **b,** Volumetric two-photon imaging (left) during random dot motion with example direction-selective units (right) for n=5 larvae. Horizontal gray bars represent stimulation epochs. Solid line and colored confidence intervals are the median and the quartile range. **c,** Reference brain-registered functionally imaged and traced WBEM neurons, showing proximity of direction-selective units and iMI inputs (filled green squares). Annotated reference brain regions have been taken from the mapZebrain atlas ((Kunst *et al.*, 2019), and **Methods**). Abbreviations: PT, pretectum; L, lateral; D, dorsal; A, anterior.

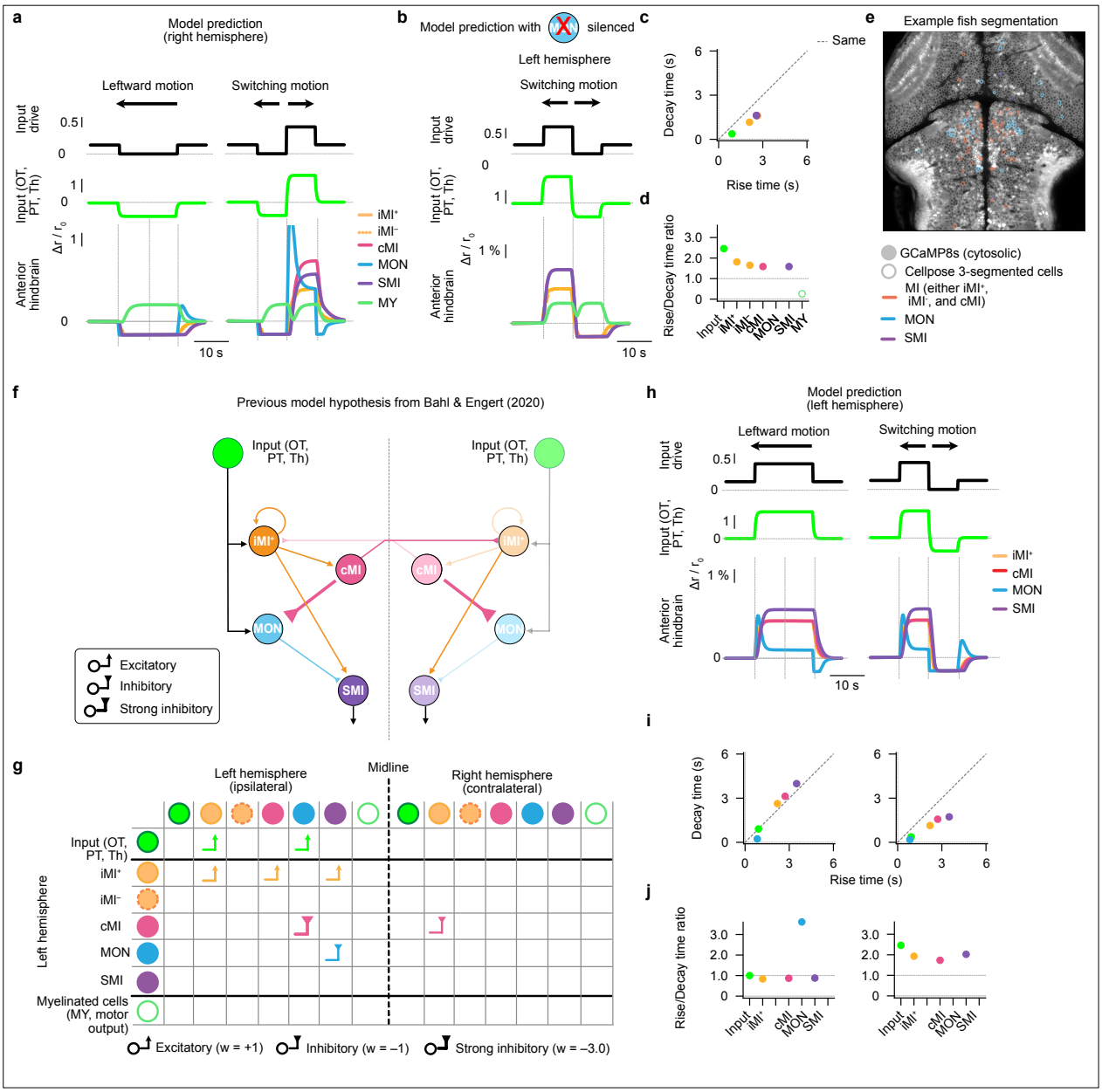

Extended Data Fig. 9 | Simulated contralateral dynamics of anterior hindbrain cell types, ablation simulations, raw imaging stack, and simulation of previously proposed network model. a, Same as in **Fig. 5d**, but for cells on the right brain hemisphere, when the motion stimulus starts moving to the left. **b,** Switching motion stimulus, as in **Fig. 5d**, for left and right brain hemispheres, for a network model in which MON cells have been silenced (rates clamped to zero). **c**, Rise and decay times (**Methods**) for all remaining model cells for dynamics in the left hemisphere (the cMI dot, red, is behind the SMI dot, magenta). **d,** Ratio of rise and decay times for all remaining model cell types. Ratios are smaller than for the case with intact MON neurons (compare to **Fig. 5f**, right). **e,** Raw average two-photon imaging plane of an example larva, exemplifying the expression of Tg(*elavl3:GCaMP8s*)^{kn6Tg} and cellpose3 segmentation results (gray contours). Segmented and functionally assigned cell types, highlighted in colored cell body contours. **f,** Connectivity diagram according to our previously proposed model (Bahl and Engert, 2020). **g,** Connectivity weight matrix as in **Fig. 5a,** but for our previously proposed model. iMI$^-$ cells have previously not been part of the model but are illustrated here for comparability. **h–j** Same quantification of dynamics as for our new model (**Fig. 5d,e,f**) but for our previously proposed one. The difference between rise and decay time is smaller compared to **Fig. 5f**.

Extended Data Table 1 | All extracted 68 neuron morphometrics used to generate our functional cell type classifier.

#	Name	Extraction strategy
1	number of contralateral branches	custom code
2	number of ipsilateral branches	custom code
3	**cable length**	navis
4	**bbox volume**	navis
5	**x_extent**	navis
6	**y_extent**	navis
7	z_extent	navis
8	**x average**	custom code
9	**y average**	custom code
10	z average	custom code
11	soma x	custom code
12	soma y	custom code
13	soma z	custom code
14	tortuosity	navis
15	n_leafs	navis
16	n_branches	navis
17	n_ends	navis
18	n_edges	navis
19	main_branchpoint	navis
20	n_persistence_points	navis
21	max_strahler_index	navis
22	sholl_distance_max_branches	navis
23	sholl_distance_max_branches_cable_length	navis
24	sholl_distance_max_branches_geosidic	navis
25	sholl_distance_max_branches_geosidic_cable_length	navis
26	main_path_longest_neurite	custom code
27	main_path_total_branch_length	custom code
28	first_major_branch_longest_neurite	custom code
29	first_major_branch_total_branch_length	custom code
20	first_branch_longest_neurite	custom code
31	first_branch_total_branch_length	custom code
32	cable_length_2_first_branch	navis
33	z_distance_first_2_first_branch	navis
34	biggest_branch_longest_neurite	custom code
35	biggest_branch_total_branch_length	custom code
36	longest_connected_path	custom code
37	n_nodes_ipsi_hemisphere	custom code
38	n_nodes_contra_hemisphere	custom code
39	n_nodes_ipsi_hemisphere_fraction	custom code
40	n_nodes_contra_hemisphere_fraction	custom code
41	**x_location_index**	custom code
42	**fraction_contra**	custom code
43	**y_extent_ipsi**	custom code
44	**z_extent_ipsi**	custom code
45	**max_x_ipsi**	custom code
46	**max_y_ipsi**	custom code
47	max_z_ipsi	custom code
48	min_x_ipsi	custom code
49	min_y_ipsi	custom code
50	min_z_ipsi	custom code
51	max_x_contra	custom code
52	max_y_contra	custom code
53	max_z_contra	custom code
54	min_x_contra	custom code
55	min_y_contra	custom code
56	min_z_contra	custom code
57	avg_delta_death_birth_persitence	navis
58	median_delta_death_birth_persitence	navis
59	std_delta_death_birth_persitence	navis
60	z_extent_contra	custom code
61	y_extent_contra	custom code
62	midline crossing x	custom code
63	midline crossing y	custom code
64	midline crossing z	custom code
65	crossing angle	custom code
66	crossing angle 2D	custom code
67	**morphology (ipsilateral or contralateral)**	custom code
68	neurotransmitter (exc., inh., or unknown)	custom code

The list of all 68 morphometrics we extracted from each cell to build our functional cell type classifier. We used the navis package to compute features directly from .swc files and developed custom code to further extend feature space. Through a feature ranking with reverse feature elimination algorithm (see **Methods**), we identified 7 feature to be the best predictor of function (highlighted in red).